NANO · MICRO small
www.small-journal.com

Multi-Component Intermetallic Nanocrystals: a Promising Frontier in Advanced Electrocatalysis

Mingjin Cui, Haijiao Liu, Bo Xu, Xinwei Shi, Qingxi Zhai, Yuhai Dou, Xiangkang Meng, Xinghui Liu,* Yu Ding, Huakun Liu, and Shixue Dou**

As the latest representation of high-entropy materials, structurally ordered multi-component intermetallic (MCI) nanocrystals exhibit various attractive functional properties, exceptionally high activity, and durability in energy-related electrocatalytic applications. These properties are primarily attributed to their ordered superlattice structures and high-entropy effects in one sublattice. However, to date, MCI nanocrystals have not been systematically studied. This review comprehensively analyzes the structural characteristics of MCI nanocrystals and the thermodynamics and kinetics of their ordering transformation. Various synthesis strategies for constructing MCI nanocrystals are discussed, including traditional thermal annealing, the cutting-edge manufacturing protocol of Joule heating methods, and wet chemical synthesis, highlighting their advantages and limitations. Importantly, the electronic structure characteristics of MCI nanocrystals are analyzed, beginning with the orbital hybridization of platinum group elements with 3*d*-block, *p*-block, and *f*-block metals, and further discussing their roles in electrocatalytic reactions (oxygen reduction reaction, hydrogen evolution reaction, formic acid oxidation reaction, and methanol oxidation reaction). The focus is on how the optimized electronic structure of active sites in MCI nanocrystals and the shifting of the *d*-band center contribute to performance enhancement. Based on comprehensive analysis, this review summarizes the progress made in MCI nanocrystals to date and highlights the significant challenges faced by the scientific community.

1. Introduction

High-entropy materials were first introduced based on the realization that traditional alloy designs, which rely on a single dominant element, were approaching their performance limits. In 2004, the novel concept of "high-entropy" alloys emerged as a promising approach to overcome this limitation.[1–3] High-entropy alloys (HEAs) typically consist of five or more elements in nearly equal atomic ratios, and bulk HEAs exhibit unique structural properties.[4–7] More notably, research on HEAs has extended from bulk materials to the nanoscale, where HEA nanocrystals[8–13] (including HEAs,[14] high-entropy oxides,[15–17] high-entropy sulfides,[18–20] high-entropy carbides,[21–23] etc.) demonstrate outstanding catalytic performance. As shown in the timeline **Figure 1**, over the past 20 years, this has sparked extensive research in the nanomaterials science community and yielded significant advancements,[24–30] particularly in the recently developed structurally ordered multi-component intermetallic (MCI) nanocrystals.[31–37] Noted that the term "MCI" denotes intermetallic compounds in a general sense, encompassing all forms, including nanocrystals and bulk materials. In this context, "MCI" specifically refers to nanocrystals unless stated otherwise. As the latest representative of multi-component nanomaterials, MCIs feature long-range ordered crystal structures, where at least one sublattice is randomly occupied by two or more atoms in near-atomic ratios. This implies that MCIs combine the high-entropy effects of HEAs with the ordered superlattice structures of classical binary intermetallic.[38] Specifically, atoms within the same sublattice occupy random positions, while atoms across different sublattices maintain overall order. This overall order is characteristic of classical binary intermetallic structural types including $L1_0$, $L1_1$, $L1_2$, B2, $L2_1$, and B35 among others.[39]

These MCI nanocrystals exhibit exceptional electrocatalytic performance, primarily attributed to the independent or synergistic effects arising from the incorporation of multiple elements within an intermetallic structure. The effects include the ligand effect, which involves charge transfer between distinct atoms near the adsorption sites on the catalyst surface, leading to

M. Cui, H. Liu, B. Xu, Y. Dou, H. Liu, S. Dou
Institute of Energy Materials Science
University of Shanghai for Science and Technology
Shanghai 200093, China
E-mail: mjcui@usst.edu.cn; shi@usst.edu.cn
M. Cui, X. Shi, Q. Zhai, X. Meng, Y. Ding
National Laboratory of Solid State Microstructures
College of Engineering and Applied Sciences
Nanjing University
Nanjing 210023, China
X. Liu
Science and Technology on Aerospace Chemical Power Laboratory
Laboratory of Emergency Safety and Rescue Technology
Hubei Institute of Aerospace Chemotechnology
Xiangyang 441003, China
E-mail: liuxinghui@casc42.cn

The ORCID identification number(s) for the author(s) of this article can be found under https://doi.org/10.1002/smll.202500306

DOI: 10.1002/smll.202500306

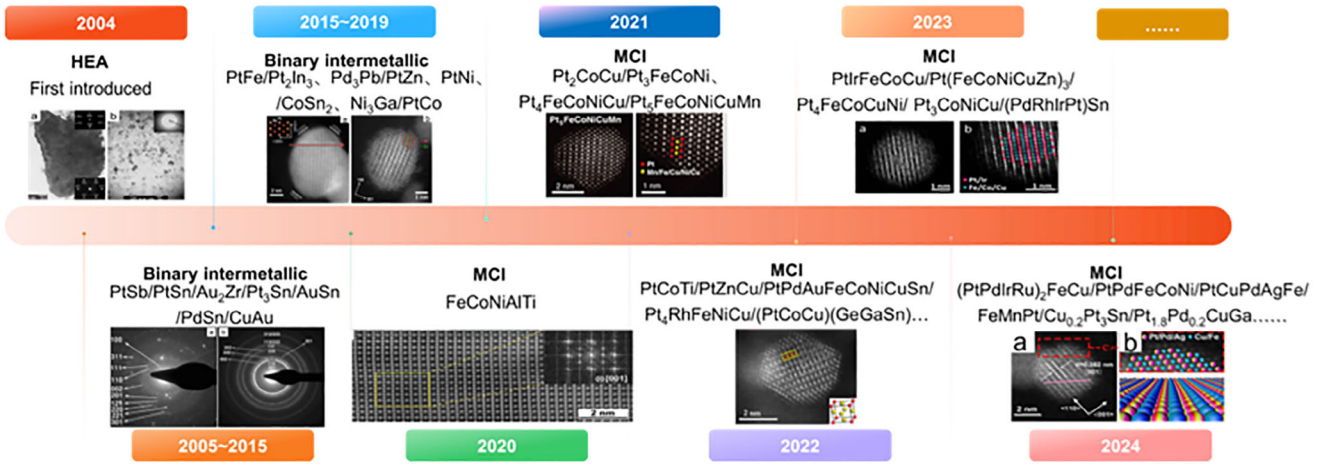

Figure 1. Evolution of research on HEAs and MCIs. Reproduced with permission.[31] Copyright 2023, John Wiley & Sons, Ltd.; Reproduced with permission.[40] Copyright 2013 Elsevier Ltd.; Reproduced with permission.[41] Copyright 2023, American Chemical Society.

alterations in the catalyst material adsorption properties; the geometric effect, which optimizes the spatial arrangement of active sites through the positioning of adjacent atoms, enhancing catalytic performance and selectivity in response to the specific reactions; and the strain effect, resulting from the incorporation of different elements with distinct atomic sizes into a common lattice, generating stress and strain fields within the MCIs.[42,43] In MCIs, these effects may function independently or interact synergistically. To this end, numerous research groups have successfully explored the manipulation of diverse high-entropy compositions in MCIs by incorporating platinum group metals such as Pt, Pd, and Au alongside 3*d* transition metals, including Fe, Co, Ni, Cu, and others. For instance, the MCI PtFeCoNiCu exemplifies the synergistic effects achievable through multiple element combinations.[33,44–46] The hybridization of 5*d* orbitals (platinum group metals) and 3*d* orbitals (Fe, Co, Ni, and Cu, and others) within these high-entropy systems facilitates effective electron redistribution, significantly enhancing catalytic performance in the oxygen reduction reaction (ORR). Most notably, in recent years, there has been growing interest in incorporating low-melting-point metals (e.g., Ga, In, and Sn), or rare earth metals (e.g., La, Ce) into MCI structures.[47–55] This incorporation is particularly noteworthy, as it facilitates the inclusion of diverse metal groups—specifically, the distinct contributions from *p*, *d*, and *f* orbitals—resulting in unique hybridization patterns and varying electron densities within the MCI structure. Such strategic integration of different metal contributions is essential for tuning catalytic properties, as it directly affects the electronic environment of the active sites, thereby influencing their reactivity and selectivity in catalytic processes.

Considering the multiple orbital hybridization states and potential synergistic effects among elements from different blocks of the periodic table, Pt-based MCI nanocrystals can be effectively classified into three categories: those that incorporate Pt with 3*d*-block transition metals, those that combine Pt with *p*-block low-melting-point metals, and those that feature Pt with *f*-block rare earth metals. Recent studies demonstrate the impact of multiple orbital hybridization on electronic structure and explore its influence on various catalytic reactions, including ORR,[36,45,56–59] hydrogen evolution reaction (HER),[45,47,60,61] formic acid oxidation reaction (FAOR),[35,62–66] and methanol oxidation reaction (MOR).[54,67–70] For example, Duan et al. reported that in $Pd_1Ni_2Ga_1$, Pd atoms become negatively charged due to electron transfer from adjacent Ni and Ga atoms.[71] This occurs because of significant hybridization among the Ni (3*d*), Pd (4*d*), and Ga (4*p*) orbitals, resulting in electrons transferring from Ga to Ni and then from Ni to Pd. Similarly, Li et al. found that $L1_0$-Pt_2CuGa intermetallic nanoparticles (NPs) exhibit strong Pt-Ga interactions, which are attributed to the *p-d* antibonding state, resulting in a robust Pt-Ga covalent bond and enhanced catalytic performance for ORR.[53] Moreover, Zhong et al. investigated the synergistic effects of 5*d*-4*d*-3*d* electron coupling in $RuLaNi_{1-x}Co_x$ MCIs, noting that the 5*d* orbital of La loses electrons, creating an electron-rich region around La, while the 4*d* orbital of Ru gains electrons.[47] The 3*d* orbitals of Ni and Co interact with the 5*d* and 4*d* orbitals of La, forming an inner electron-deficient region and an outer electron-rich annular region.

Driven by their tunable electronic structure for optimizing electrocatalytic reactions, MCI nanocrystals have become a focal point of active research over the past two decades. Synthetic methods for the production of MCI nanocrystals have been developed, including thermal annealing in reducing or inert atmospheres at temperatures below the ordered to disordered phase transition point.[33,46,48,49,56–59,70,72–80] Other methods involve Joule heating,[32,81] rapid and complete homogeneous mixing followed by a short period of rapid ordering, and various wet chemistry methods. These wet chemistry methods include seed-mediated diffusion growth utilizing preformed seeds, as well as direct one-pot syntheses that involve the simultaneous reduction and/or decomposition of multiple metal precursors.[55,60,82,83] Among these methods, annealing is the most widely employed due to its simplicity. However, a major challenge during annealing is the trade-off between particle growth and achieving a high-order degree. While increasing the temperature can enhance the particle's order degree, it also leads to larger particle sizes, which is generally undesirable. To address this issue, several strategies, including sulfur,[33] or boron anchoring,[46] low-melting-point metal doping,[48–51,53,68,71,72] and rapid Joule heating methods[81]

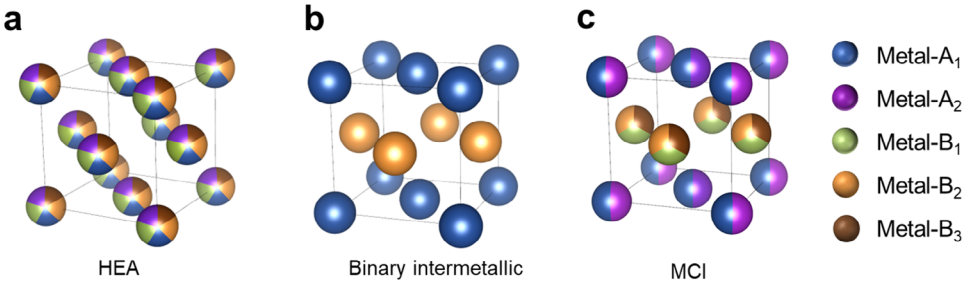

Figure 2. Schematic diagram illustrating the atomic arrangement in typical alloys. The atoms of different colors represent different element species, labeled as A_1, A_2, B_1, B_2.... a) Quinary HEA. b) Classical binary $L1_0$-type intermetallics. c) Quinary $L1_0$-type MCI. Reproduced with permission.[38] Copyright 2024, Elsevier.

have been proposed to achieve high-order and ultra-small MCI nanocrystals.[48–51,53,68,71,72]

Therefore, in this review, we aim to provide a foundation for the general guidelines and strategies for the novel MCI nanocrystals by analyzing the reported parameters, such as mixing entropy and mixing enthalpy, as well as the thermodynamics and kinetics of the ordering process. Additionally, we will investigate the impact of different orbital hybridizations (3*d* orbital, 5*d* orbital, and 4*p* orbital) and changes in electronic structure on the performance (including activity and stability) of MCI nanocrystals in small molecule catalytic reactions, an aspect that has not been systematically considered in previous literature.

2. Structure Features, Entropy, and Enthalpy of MCIs

2.1. Structure Features

High-entropy materials are defined as those containing at least five principal elements in nearly equal atomic ratios. Yet, ternary and quaternary systems can be considered high-entropy materials under certain conditions, particularly when they exhibit similar properties to high-entropy materials.[84,85] HEA nanomaterials have garnered significant attention across various research fields due to their distinctive structure and superior physical and chemical properties (**Figure** 2a).[86–89] As a recent advancement within this paradigm, structurally ordered MCI nanocrystals exhibit exceptional and desirable functional properties, primarily stemming from the unique formation of intermetallic phases in multi-component systems. In contrast to HEAs, which are compositionally complex but exhibit a disordered distribution of constituent elements, MCIs maintain compositional complexity while showcasing an ordered arrangement of multiple elements. The crystal structure of MCIs generally follows that of their classical binary intermetallic compounds. Figure 2b illustrates a classical binary intermetallic compound, where a single element occupies each sublattice. The entropy of such phases is typically negligible. However, MCIs often have more components than sublattices, resulting in each sublattice being occupied by two or more metallic elements with similar characteristics (e.g., radius and electronegativity). For instance, the crystal structure of $(A_1A_2)_1(B_1B_2B_3)_1$ MCI resembles the A_1B_1 structure of its classical binary intermetallic compound $L1_0$, with a random distribution of elements A_1 and A_2 on one sublattice and elements B_1, B_2, and B_3 randomly on the second sublattice (Figure 2c).[35,48,49]

The classical binary intermetallic compound $L1_0$ (space group P4/mmm, CuAu type, e.g., PtFe, PtCo, PtZn) primarily originates from the face-centered cubic (*fcc*) structure. Additionally, typical *fcc*-derived intermetallic structures include $L1_0$, $L1_1$ (space group $R\bar{3}m$, PtCu type, e.g., PtCu), and $L1_2$ (space group $Pm\bar{3}m$, Cu_3Au type, e.g., Pt_3Co, Pt_3 Zn, Pt_3Sn), as shown in **Figure** 3. Furthermore, the typical body-centered cubic (*bcc*)-derived intermetallic structure includes B2 (space group $Pm\bar{3}m$, CsCl type, e.g., PdCu, FeRh), $L2_1$ (space group $Fm\bar{3}m$, Cu_2MnAl type, e.g., Fe_2CrGa, Cu_2MnSn). Additionally, hexagonal close-packed (*hcp*)-derived B35 (P6/mmm, CoSn type) intermetallic structure. Among the reported Pt-based intermetallic nanocrystals, $L1_0$ and $L1_2$ are the most common structures. The $L1_0$ structure can be regarded as a tetragonal distortion of the *fcc* structure, alternating atomic layers of two elements with a 1:1 stoichiometric ratio along the *c*-axis. In the $L1_2$ structure, two elements with a 3:1 stoichiometric ratio occupy the positions in the *fcc* lattice, where the element with the higher atomic ratio is at the face-centered positions and the other at the vertices.

2.2. Mixing Entropy and Mixing Enthalpy of MCIs

In thermodynamics, entropy is a critical parameter that quantifies the state of disorder within a system. MCIs are characterized by an ordered superlattice structure and a significant high-entropy effect within their sublattice. This structural behavior is fundamentally different from that of HEAs, even when comprised of similar components, due to the unique structural characteristics inherent to MCIs. The structural formula of MCI can be expressed as $(A_1, A_2, A_3, ..., A_x)_m(B_1, B_2, B_3, ..., B_y)_n$, where x and y denote the element species in sublattices A and B, respectively, m and n are the stoichiometric ratios. To estimate the MCI configuration entropy based on the sublattice model, the following equation can be used:[4]

$$S_{mix}^{HEI} = -R\left[n^A\sum_{i=1}^{x} f_i^A ln\left(f_j^A\right) + n^B\sum_{j=1}^{y} f_i^B ln\left(f_j^B\right)\right] / \left(f^A + f^B\right) \quad (1)$$

where R is the ideal gas constant (8.314 $J{\cdot}mol^{-1}{\cdot}K^{-1}$), n^A or n^B represents the number of sites in sublattice A or B, and $f^A{}_i$ or f

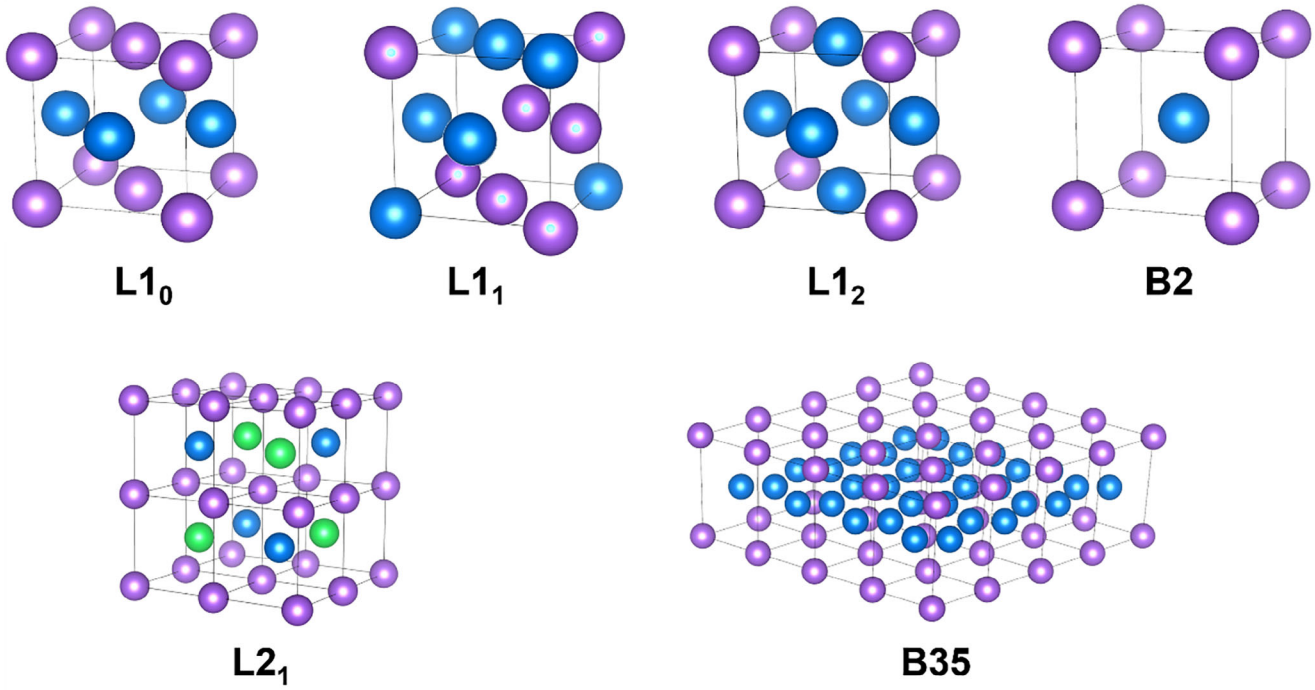

Figure 3. Classical intermetallic structures, i.e., $L1_0$, $L1_1$, $L1_2$ derived from *fcc*; B2, $L2_1$ derived from *bcc*; B35 derived from *hcp*.

$^{B}{}_{j}$ is the molar fraction of the i or j component in their respective sublattices. For instance, consider the sublattice configuration shown in Figure 2c: $(A1, A2)_1(B1, B2, B3)_3$, which consists of two sublattices, A and B. The number of sites in sublattices A and B are $n^A = 1$ and $n^B = 3$, respectively. The fraction of element species x on each sublattice $f^{A}{}_{i}$ is the reciprocal of the number of atomic species s n^A. Since there are two species of atoms (A_1, A_2) on sublattice A, $f^{A}{}_{i} = 1/2$; and there are three species of atoms (B_1, B_2, B_3) on sublattice B, $f^{B}{}_{j} = 1/3$.

Mixing enthalpy is another critical parameter, useful for assessing the potential for intermetallic compound formation.[4] A more positive mixing enthalpy implies lower miscibility of components, leading to a higher tendency for component segregation. Conversely, a more negative mixing enthalpy between different components indicates a stronger binding force between elements, promoting intermetallic compound formation.

2.3. Thermal Dynamic and Kinetic Perspectives

The synthesis of MCI nanocrystals marks a significant advancement in nanomaterials science, yet it also presents substantial challenges. One major obstacle is the high activation energy required for interdiffusion and equilibration among the multiple components—a critical step for achieving the desired ordered atomic arrangement. This challenge is compounded in MCIs by the difficulty of experimentally determining the occupancy and distribution of multiple elements within a single sublattice and by the added complexity of elucidating the equilibrium relationship between the short-range and long-range order of these elements.[90] Integrating insights from both thermodynamics and kinetics is essential for overcoming these hurdles.

2.3.1. Thermodynamic Perspectives

The thermodynamic perspective highlights the importance of Gibbs free energy (G), which is influenced by enthalpy (H), entropy (S), and temperature.[24,91–93] According to the equation:[94]

$$G = H - TS \tag{2}$$

The stability of a given nanocrystal is determined by achieving the lowest Gibbs free energy state. The difference in energy between the two states drives the transition from a disordered to an ordered phase. At higher temperatures, the disordered HEA is more stable than the ordered MCI. This stability arises because the entropy of the disordered atomic arrangement is higher, dominating the total free energy at elevated temperatures.[91] Conversely, at lower temperatures, the enthalpy term predominates in the free energy contribution, and the stronger bonding between $A(A_1, A_2, A_3,...)$ and $B(B_1, B_2, B_3,...)$ atoms favors the formation of a thermodynamically stable MCI phase. Disordered HEA possesses higher entropy compared to MCI, resulting in a negative TS. Hence, at high temperatures, the disorder-to-order transition is unfavorable. At lower temperatures, H dominates in G , and H is composition and bond energy dependent.[95–97] In MCI structures, the strong d orbital interaction between atoms A_1, A_2, A_3, ...A_x on sublattice A and atoms B_1, B_2, B_3, ...B_y on sublattice B results in negative H. The metal species and compositions on sublattices A and B determine H, and consequently G.

Therefore, similar to binary classical intermetallic compounds, the metal species and compositions on each sublattice in MCIs play a crucial role in the disorder-to-order transition. The formation of intermetallic compounds requires specific ratios of atoms on each sublattice, and the interactions among multiple elements are complex, necessitating precise control over the species and compositions of the metals involved.

2.3.2. Kinetic Perspectives

From a kinetic standpoint, the ordering dynamics in MCIs depend on a delicate balance between the thermodynamic driving force—the energy difference between the disordered and ordered states—and the activation barrier that must be overcome for atomic rearrangement. This transformation is controlled by both the rate at which the ordered phase forms and the rate at which atoms diffuse to enable this transition. A significant challenge in studying these processes is the experimental difficulty of capturing the transient intermediate states that occur during atomic diffusion. The disorder-to-order transition is inherently slow because it requires breaking strong metal–metal bonds, which imposes a high activation barrier.[90]

One effective strategy to overcome this challenge is to increase the concentration of vacancies within the disordered alloy. A higher vacancy concentration lowers the energy barrier for atomic migration, thereby promoting the phase transition and facilitating the formation of an ordered structure. Our research has demonstrated that enhancing the vacancy concentration in disordered alloys can significantly accelerate the transition to an ordered state.[98] Another approach is to raise the annealing temperature, which also enhances atomic diffusion. However, this strategy must be applied judiciously because higher temperatures can lead to the coalescence of nanoparticles into larger particles, reducing the overall surface area—a drawback that is particularly critical for electrocatalytic applications.

Particle size further influences the kinetics of ordering. Smaller particle sizes are associated with a reduced driving force. However, smaller particle sizes exhibit a higher trend for diffusion and formation of ordered structures. Consequently, the observed trends suggest a critical size that facilitates the formation of ordered intermetallic. This phenomenon was demonstrated in our work on the synthesis of $Pt_1(FeCoNiCu)_1$-MCI.[32] The critical particle size for $Pt_1(FeCoNiCu)_1$ was 4–5 nm. Particles larger than this size exhibit a lower degree of ordering or require extended treatment times to achieve increased ordering. Furthermore, even larger particles may even undergo phase separation.

In summary, the kinetics of the disorder-to-order transition in MCIs are determined by the interplay between the thermodynamic driving force and the activation barrier for atomic diffusion. Strategies such as increasing vacancy concentration, optimizing annealing temperature, and controlling particle size are all effective in enhancing atomic migration and promoting order. Nonetheless, due to the complexity of these systems, further systematic experimental validation and refinement are necessary to fully understand and engineer MCIs with the desired properties.

2.4. Different MCI Effects

2.4.1. Ligand Effect

The ligand effect refers to the charge transfer between different atoms near the adsorption site on the catalyst surface, which alters the catalyst's adsorption properties and overall reactivity[99] In MCIs, introducing multiple metals, such as Pt combined with various 3*d* transition metals, into sublattices leads to significant electronic modifications. Specifically, in $L1_0$ (Pt-3*d*) MCIs, electrons are transferred from the less electronegative 3*d* transition metals to Pt, causing a downward shift in Pt *d*-band center away from the Fermi level (**Figure 4a**). This shift significantly influences the binding energies of adsorbates, such as intermediates in catalytic reactions, and modifies the electronic structure of the active sites.[100,101] Unlike binary intermetallics, where this effect is more limited, the presence of multiple metals in MCIs allows for fine-tuning of electron transfer, optimizing catalytic performance for specific reactions. The variation in the extent of this shift, depending on composition, shows that MCIs can offer a greater range of flexibility compared to HEAs, which do not exhibit the same level of control over the d-band shift. Adjusting the distribution of transition metals within the sublattice enables researchers to achieve a more precise balance of activity, selectivity, and stability in catalytic processes, underlining the importance of the ligand effect in MCI development.[102]

For instance, Wang et al.[35] demonstrated that in the MCI-$(PtPdIrRu)_2FeCu$, electrons are transferred from Fe/Cu to Pt through the ligand effect, resulting in the downward shift of the *d*-band center of Pt and weakening the binding of intermediates like CO*. This shift facilitates FAOR via the direct electrooxidation pathway and enhances the FAOR activity of the MCI. Similarly, Xia et al.[36] showed that electron transfer due to the ligand effect occurs in PFCNCZ-MCI, where electrons are transferred from non-precious metals to Pt. The stronger electronegativity of platinum leads to the transfer of outer electrons from non-precious metals (such as Fe, Zn, Co, Ni) to Pt, reducing the outer electrons of the non-precious metals and increasing those of Pt. This effect causes Zn atoms, originally with filled outer electron orbitals, to appear as having empty orbitals, making them more conducive to binding with oxygen. This, in turn, regulates non-precious metal sites to become highly active sites for ORR, significantly improving the ORR catalytic activity of PFCNCZ-MCI. This highlights the crucial role of the ligand effect in enhancing catalytic properties through electronic modulation.

2.4.2. Geometric Effect

The integration of multiple metals into the sublattice of MCI nanocrystals significantly alters the geometric configuration of the catalyst surface, which in turn impacts the catalytic behavior.[103,104] For instance, when Pt is combined with transition metals such as Fe, Co, Ni, and Cu, a variety of Pt atom configurations are formed on the surface, including isolated Pt atoms, Pt pairs, and Pt clusters (Figure 4b). These different configurations influence the adsorption behavior and catalytic properties of the material in distinct ways. In the case of isolated Pt sites, adsorbates interact primarily with the top sites

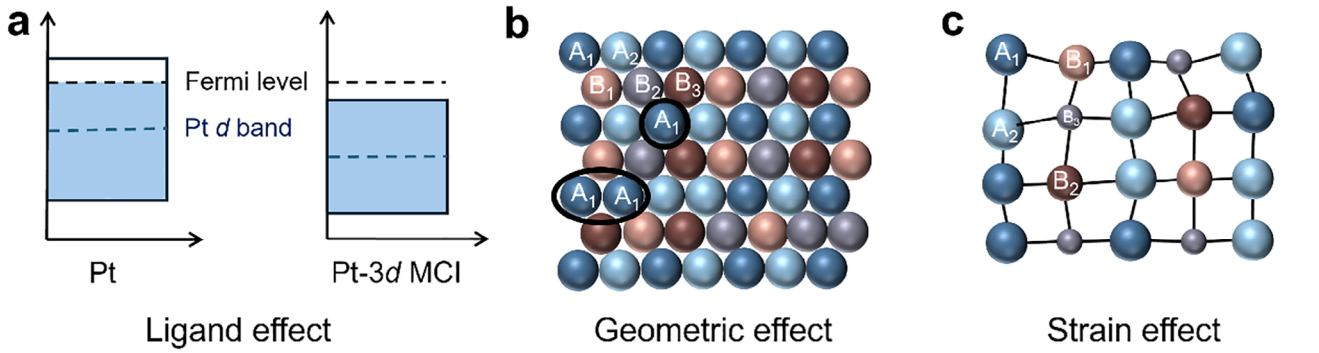

Figure 4. a) In $L1_0$ (Pt-3*d*) MCI, electrons transfer to the element with high electronegativity, changing the electronic structure of the metal surface, and making the *d*-band center deviate from the Fermi level. b) Illustration of the changes in the geometry of the nanocrystal surface. Atom layers of B_y can isolate that of A_x. c) Different atom sizes in MCI result in strain effects.

of the catalyst, resulting in single-site behavior. In contrast, Pt pairs enable bridging adsorption, where adsorbates interact between the two Pt atoms, allowing for different reaction pathways. Furthermore, Pt clusters, which consist of three Pt atoms, provide even greater complexity, enabling reactant molecules to be adsorbed and activated from multiple directions, thereby supporting more intricate catalytic reactions. This ability to manipulate the geometric arrangement of Pt atoms through the strategic incorporation of 3*d* transition metals gives MCIs a distinct advantage over binary alloys, whose surface configurations are less versatile and harder to fine-tune for precise catalytic optimization.[105]

A specific example is seen in the structure of MCI, where isolated Pt sites are created. The geometry of these active sites plays a crucial role in the adsorption and desorption behavior of propylene on the catalyst surface.[49] Due to the isolation of Pt atoms, the adsorption of propylene on the MCI surface is weakened, making it easier for propylene to desorb. This property enhances both the selectivity and stability of the catalyst, as the weak adsorption prevents unwanted side reactions and promotes more efficient catalytic cycles.

2.4.3. Strain Effect

The strain effect plays a vital role in the properties of MCI nanocrystals. The presence of multiple elements in MCIs leads to varying atomic sizes, which induce lattice distortions and result in pronounced strain effects (Figure 4c). Unlike traditional alloys, where the lattice typically undergoes less distortion, the random arrangement of different elements in MCIs disrupts the regular lattice, creating more significant strain. This strain is not only limited to the bulk properties but also affects the surface and defect states, where unique electron densities and energy levels emerge compared to the bulk material. These strain-induced changes can modify the electronic structure, create energy gaps, alter d-band widths, and introduce localized states, all of which are crucial for electrocatalytic activity.[106] The strain effect in MCIs offers more flexibility and potential for optimization in catalytic reactions compared to binary alloys. However, understanding and quantifying this strain effect remains challenging due to difficulties in directly observing these distortions. Further research is needed to measure lattice distortions, correlate them with the atomic radii of constituent elements, and explore how strain impacts the electronic structure and catalytic performance. Since both the ligand and strain effects influence the d-band, distinguishing between their individual roles can be complex, but their combined impact is essential in enhancing the catalytic properties of MCIs.

For instance, Li et al.[53] demonstrated that the introduction of Ga into the PtCu lattice induces a directed covalent atomic interaction between Pt and Ga, resulting in a transition from the $L1_1$ phase to the $L1_0$ phase, thereby reducing the over-compressive strain in $L1_1$-PtCu. Their study also shows that doping with Pd can cause strain effects; in $Pt_{(2-x)}Pd_xCuGa$, increasing the Pd content leads to a larger positive shift of X-ray diffraction peaks to a higher angle, indicating that compressive strain in the lattice can be adjusted by altering the Pd content. The extended X-ray absorption fine structure spectra reveal that the Pt—M bond length in $Pt_{1.8}Pd_{0.2}CuGa/C$ (2.28 Å) is shorter than that of Pt_2CuGa/C (2.35 Å) and Pt—Pt bond length in Pt foil (2.51 Å), suggesting that this induces compressive strain, increases the orbital overlap of Pt atoms with surrounding metal atoms, and shifts the d-band center away from the Fermi level. This shift weakens the interaction of the catalyst surface with adsorbed intermediates, thereby enhancing the MOR kinetics. Similarly, Liang et al.[44] reported that the $Pt(FeCoNiCu)_3$ catalyst they prepared exhibited remarkable intrinsic activity, attributed to enhanced compressive strain effects of up to 9.82%, optimizing the adsorption of ORR intermediates.

3. Synthesize Strategies and Characterization

3.1. Thermal Annealing

The controllable incorporation of multiple elements into a well-defined MCI nanocrystal structure remains a challenge. A significant challenge is the tendency for particle size to increase, leading to agglomeration and sintering at elevated temperatures. The primary mechanisms of particle agglomeration are coalescence and Ostwald ripening.[93] Coalescence involves the

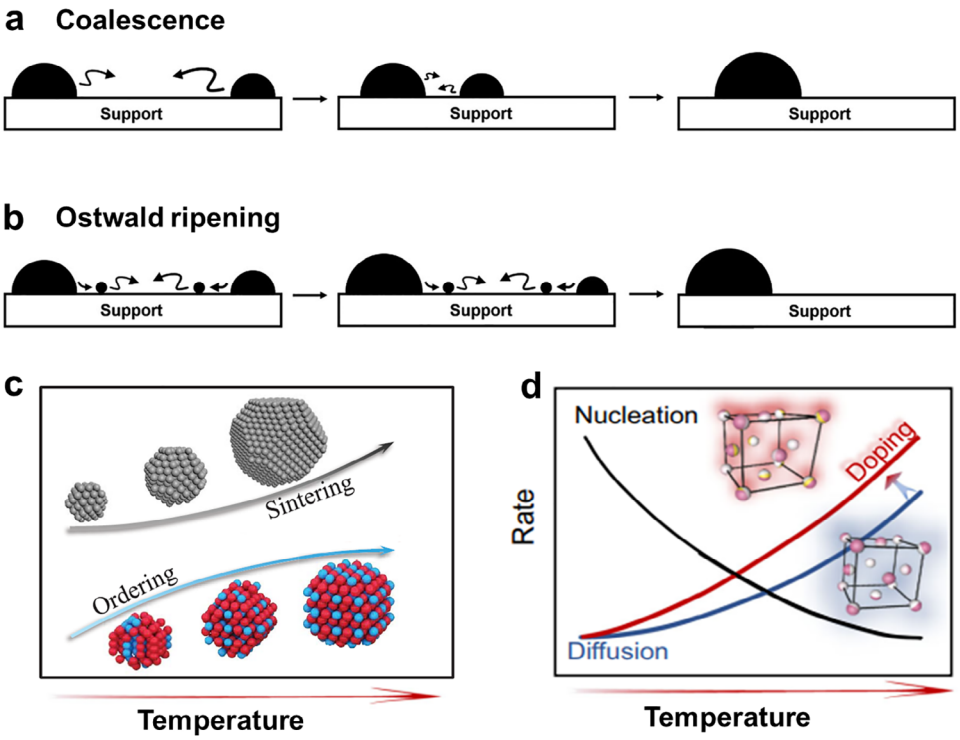

Figure 5. Schematic illustrations of the two principal sintering mechanisms or pathways for inter-particle sintering: a) Coalescence and b) Ostwald ripening, respectively. Reproduced with permission.[93] Copyright 2018, The Royal Society of Chemistry. c) Schematic illustration showing the dilemma of simultaneously accelerated sintering kinetics and atom ordering kinetics with temperature. Reproduced with permission.[33] Copyright 2021, AAAS. d) Illustration showing the dependence of nucleation and diffusion kinetic rate on temperature in the disorder-to-order transition. Reproduced with permission.[50] Copyright 2023, Nature Publishing Group.

migration of metal particles on the support surface through Brownian motion, culminating in their coalescence into larger particles (**Figure 5**a). This process accelerates when the metal-support interaction is weak, and the inter-particle distance is small. Ostwald ripening, on the other hand, occurs when there is a chemical potential (particle size) difference between particles, causing smaller particles to dissolve and redeposit on larger particles (Figure 5b). These mechanisms may act simultaneously or alternately during the sintering process. Potential strategies to address these challenges include enhancing metal-support interaction, increasing inter-particle distances, and/or ensuring a uniform size distribution, etc.

Furthermore, synthesizing highly ordered MCI nanocrystals poses a fundamental challenge due to the competing thermodynamic driving forces and kinetic barriers during the disorder-to-order transformation. High-temperature annealing promotes ordering but inevitably leads to sintering (Figure 5c).[33] Conversely, low-temperature annealing can enhance the thermodynamic driving force for the nucleation of ordered phases in disordered HEA by staying below the critical temperature of the phase transition. However, low temperatures hinder atomic diffusion. The balance between nucleation, diffusion, and annealing temperature unavoidably results in a slow disorder-to-order transformation rate (Figure 5d). Despite these challenges, recent research has made some progress in addressing these issues.[33,50,52,107]

Wang et al. successfully synthesized MCI, such as $L1_0$-$(PtPdIrRu)_2FeCu$[35] and $L1_2$-$Pt(FeCoNiCuZn)_3$,[108] achieved by annealing at 700 °C following impregnation reduction (**Figure 6**a). In their study on $L1_2$-$Pt(FeCoNiCuZn)_3$ MCI, the high-resolution transmission electron microscopy (HR-TEM) analysis revealed lattice spacings of 0.36 nm (Figure 6b), corresponding to the superlattice plane (001), with an average particle size of ≈5.75 nm (Figure 6c). Despite achieving a relatively small particle size, the long-range order in the particle arrangement remained limited to 66.3% (Figure 6d). Although higher temperatures can enhance particle ordering, they also induce particle agglomeration, primarily through sintering or Ostwald ripening mechanisms. This underscores the inherent trade-off between achieving high order and maintaining small particle sizes.

To overcome this challenge, Liang et al. developed a sulfur-anchoring strategy to enhance the interaction between the Pt-based MCI nanocrystals and supports.[33] This method exploits the strong chemical interaction between Pt and sulfur-doped carbon supports, significantly inhibiting MCI nanocrystals sintering below 1000 °C (Figure 6e,f). This approach allowed atomically ordered nanocrystals to form with an average size of less than 5 nm at elevated temperatures. The researchers tested the high-temperature antisintering of sulfur-doped carbon support by annealing single metal Pt, finding that even after annealing at 1000 °C, the average diameter of the Pt nanocrystals remained below 5 nm. This anti-sintering capability enabled small MCI

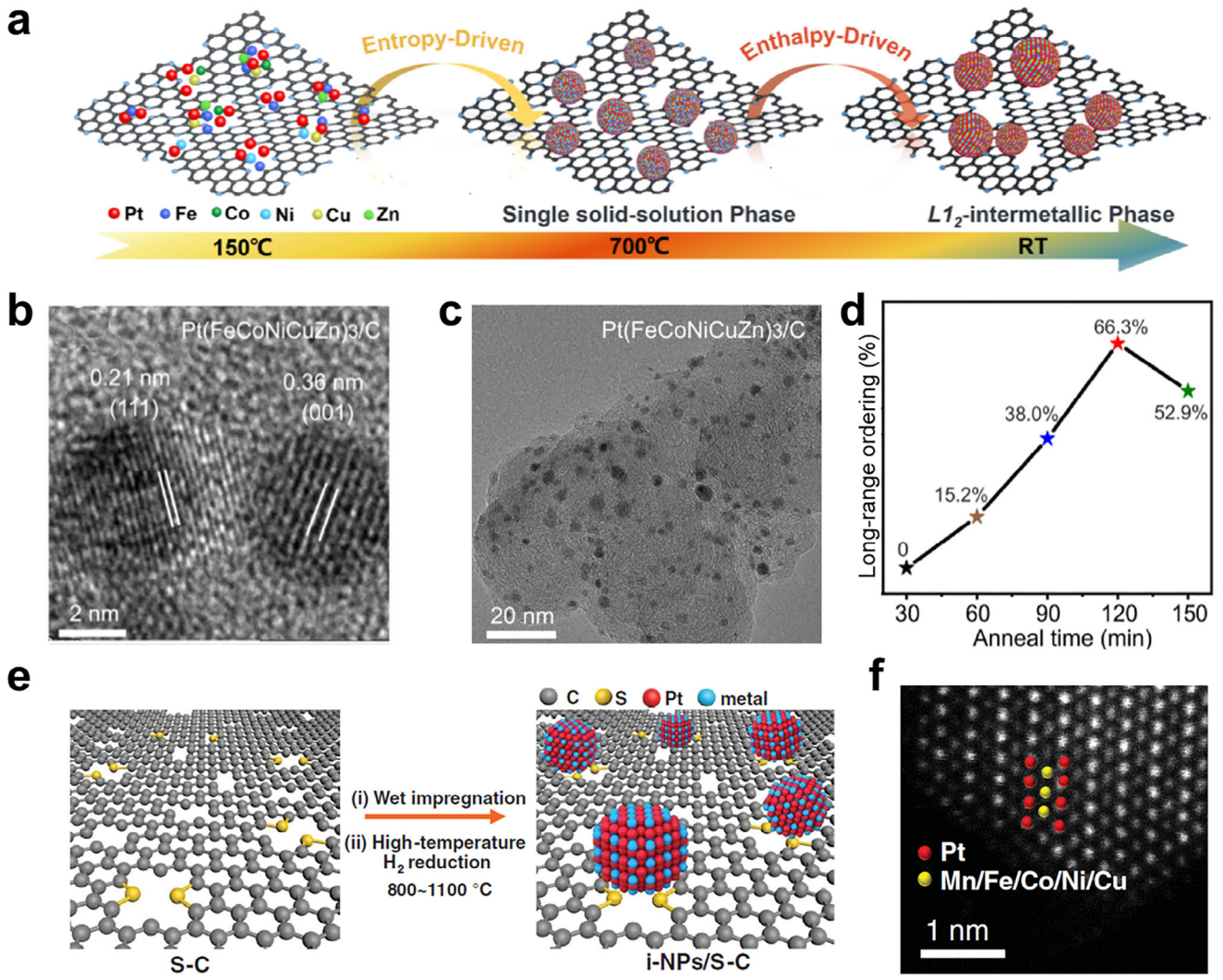

Figure 6. a) Schematic illustration for preparing $L1_2$-Pt(FeCoNiCuZn)$_3$/C. b) HR-TEM image. c) Overview TEM image. d) Calculated long-range order parameter of Pt(FeCoNiCuZn)$_3$. Reproduced with permission.[108] Copyright 2023, Elsevier. e) Schematic of the high-temperature sulfur-anchored synthesis process. f) Atomic-resolution high-angle annular dark-field scanning transmission electron microscopy (HAADF-STEM) of $L1_0$-Pt$_5$(FeCoNiCuMn)/C. Reproduced with permission.[33] Copyright 2022, AAAS.

nanocrystals to be prepared on sulfur-doped carbon support carriers through high-temperature annealing.

The strategies effectively address the challenges of high-temperature annealing. Additionally, low-temperature annealing offers a promising alternative. Similarly, Liang's research group proposed a low-melting-point metal doping strategy to reduce the ordering annealing temperature.[50] They discovered that the ordering degree of low-melting-point metal PtCo catalysts depends on the melting point of the doped metal (**Figure** 7a). As the melting point of the metal decreases, the ordering degree of low-melting-point metal-doped PtCo catalysts increases. Theoretical analysis indicates that low-melting-point metal doping reduces the atomic diffusion barrier (Figure 7b). The group successfully synthesized highly ordered $L1_0$-type Ga-doped PtCo MCI electrocatalysts (Figure 7c). Furthermore, Li and Guo et al. also reported a bond-strength weakening strategy induced by low-melting-point metal (such as Sn, Ga, In), which reduces the energy required to break the bonds between atoms and their neighboring atoms (Figure 7d),[52] thereby facilitating the ordering process of PtM (M═Ni, Co, Fe, Cu, Zn) electrocatalysts (Figure 7e). They achieved an ordering temperature as low as 450 °C, attaining ≈76% ordering after 60 min while maintaining a particle size around 3.5 nm (Figure 7f). This study revealed the fundamental mechanism by which Sn promotes the ordering process at low temperatures, including bond-strength reduction through Sn doping (Figure 7g), formation of low-coordination surface-free atoms, and rapid coalescence, effectively overcoming the trade-off between ordering degree and particle size. Although conventional high-temperature annealing methods have successfully enabled the synthesis of MCIs, the disorder-to-order conversion process still presents challenges in achieving controlled shapes for MCI nanocrystals. Furthermore, the ordering process often necessitates extended thermal annealing due to the slow interdiffusion rates of multiple elements in MCI.

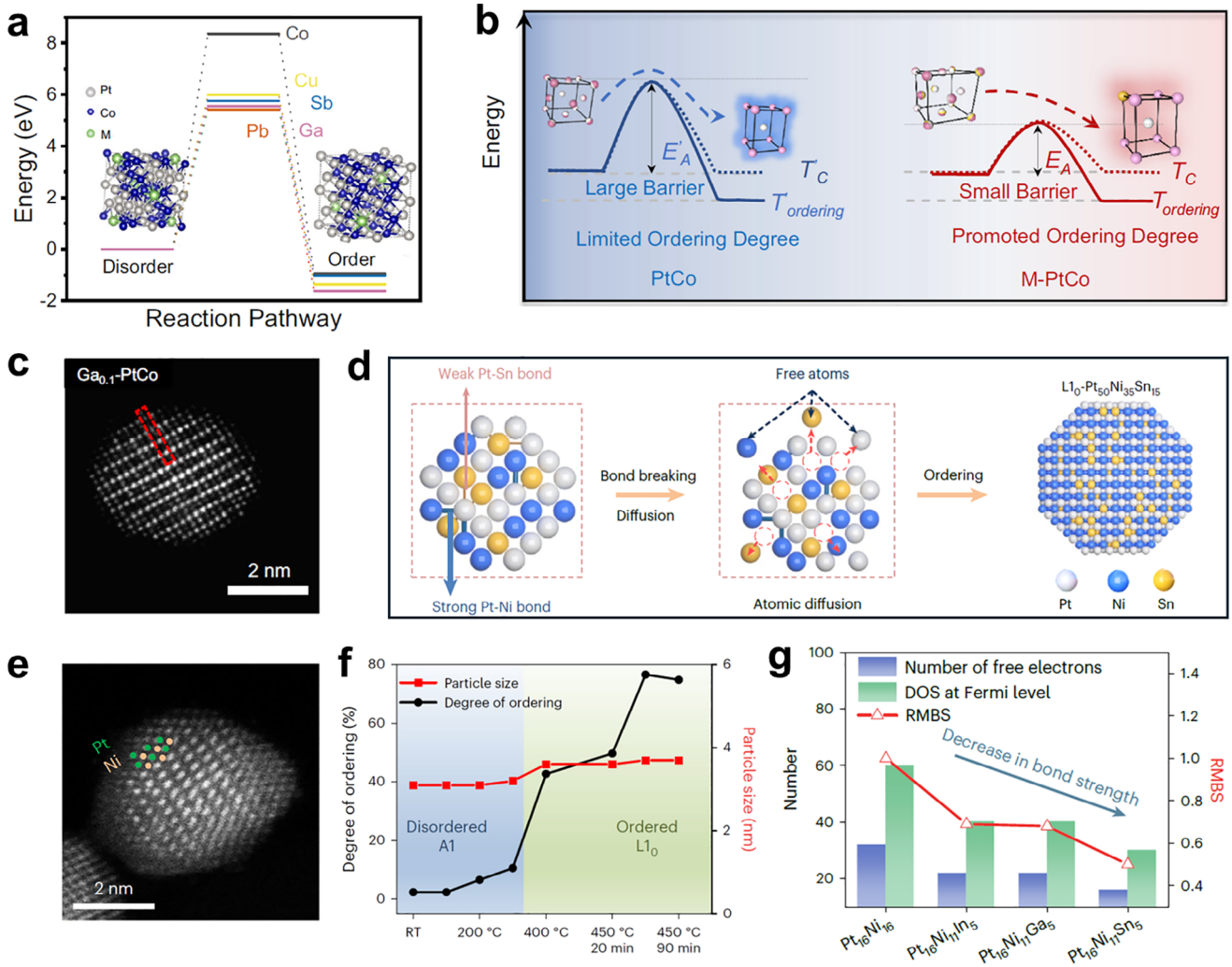

Figure 7. a) Density functional theory (DFT) calculation shows the decreased energy barrier of disorder-to-order phase transition with the low-melting-point metal doping. b) Schematic illustration showing the smaller barrier of disorder-to-order transition for M-PtCo compared to PtCo. c) Atomic-resolution HAADF-STEM images of untreated $Ga_{0.1}$-PtCo NPs. Reproduced with permission.[50] Copyright 2023, Nature Publishing Group. d) Schematic of the Sn-facilitated ordering process. e) Atomic-resolution HAADF-STEM images of $L1_0$-$Pt_{50}Fe_{45}Sn_5$. f) Ordering degree and particle size of $Pt_{50}Ni_{35}Sn_{15}$/C as a function of the annealing process. g) Statistic of the number of free electrons, electron density of states (DOS) at the Fermi level, and relative metallic bond strength values of the corresponding PtNiM system. Reproduced with permission.[52] Copyright 2024, Nature Publishing Group.

3.2. Joule Heating Method

In contrast to previously mentioned approaches that achieve a balance between particle size and order through sulfur anchoring and the annealing of low-melting-point metal dopants, emerging advanced techniques—such as Joule heating, microwave synthesis, and so on—demonstrate promising potential for improved synthesis outcomes. Specifically, our research group has employed Joule heating techniques to achieve precise control over particle synthesis, optimizing both size and order through tailored thermal profiles.[32] This technique enables rapid heating, facilitating the simultaneous decomposition of multiple metal salts to form disordered solid solution HEAs. Utilizing HEAs as precursors, this process can concurrently accelerate r_1 (Equation (7)) and r_2 (Equation (8)) at high temperatures, thus overcoming the kinetic limitations of the order-disorder transformation and rapidly reconstructing into a fully ordered MCI structure (**Figure 8a**). This method not only effectively addresses the mutual constraints between particle size and order degree, but also facilitates the exploration of new compositional spaces, enabling the synthesis of MCI nanocrystals with quinary compositions such as $Pt_1(FeCoNiCu)_1$ (Figure 8b) and even octonary compositions like $(PtPdAu)_1(FeCoNiCuSn)_1$ (Figure 8c). By precisely controlling the heating time and temperature, the issues of particle growth and aggregation associated with slow heating/cooling rates in traditional annealing are effectively mitigated, enabling the synthesis of ultra-small particle size measuring 4–5 nm. Simultaneously, experimental and Monte Carlo simulation results confirm that the critical size is 4–5 nm (Figure 8d), consisting of thermodynamic prediction about the interplay between r_1 and

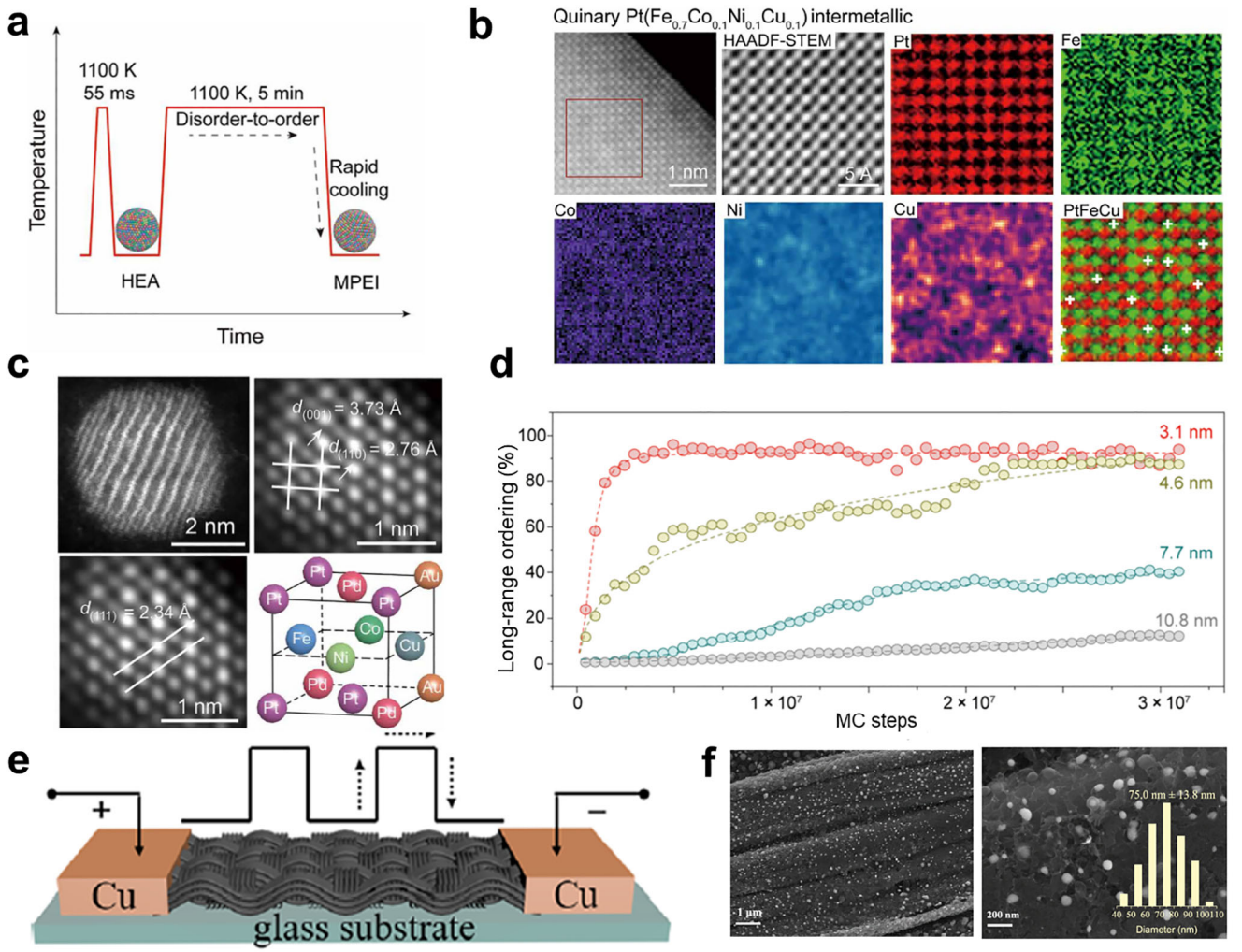

Figure 8. a) The formation of the MCI NPs in the Joule-heating process, with the temperature evolution as a function of the heating time. b) HAADF-STEM and Energy-dispersive X-ray (EDX) elemental mapping images of a quinary $Pt_1(FeCoNiCu)_1$ MCI NPs. c) An octonary $(PtPdAu)_1(FeCoNiCuSn)_1$-MCI NP along with its lattice structure. d) The long-range order of NPs varied with the Monte Carlo simulation step. Reproduced with permission.[32] Copyright 2022, AAAS. e) Schematic for preparation of the NiFeCr intermetallic integrated electrodes. f) Characterization images of the NiFeCr. Reproduced with permission.[81] Copyright 2022, American Chemical Society.

r_2, indicating a critical size. Furthermore, the ordering process is driven by the reduction of Gibbs free energy dominated by low enthalpy, which differs from the entropy-driven in the formation of HEA.[14]

Other research teams have also employed Joule heating or microwave heating for intermetallic nanocrystal synthesis. For instance, Du et al. synthesized ternary Ni_3 Fe_{1-x} Cr_x (Figure 8e,f),[81] and Tang et al. synthesized binary PtMn intermetallic compounds.[109] As an innovative synthesis technology, Joule heating has demonstrated broad application prospects in MCI nanocrystal synthesis. Notably, it can surmount thermodynamic and kinetic limitations, achieving a rapid ordering process, thus significantly advancing the development of complex MCI nanomaterials.

Joule heating provides a rapid and energy-efficient method for synthesizing MCIs by utilizing electrical resistance to generate localized high temperatures. This enables phase formation and atomic diffusion within seconds to minutes. Unlike conventional annealing methods, Joule heating allows for precise control over temperature and heating rates, which effectively minimizes the formation of undesired secondary phases and prevents particle agglomeration. In contrast to wet chemistry methods, which provide excellent compositional control at the nanoscale and enable uniform element distribution. Wet chemistry techniques excel in producing small, highly uniform MCI nanoparticles, they often involve complex multi-step processing, solvent usage, and post-synthesis annealing, which may introduce additional defects or phase instability. Detailed discussion will be provided in the following 3.3 sections.

3.3. Wet Chemistry Method

As a widely used method for synthesizing nanocrystals, the wet chemical method offers superior control over morphology and ensures uniform size distribution in producing metallic

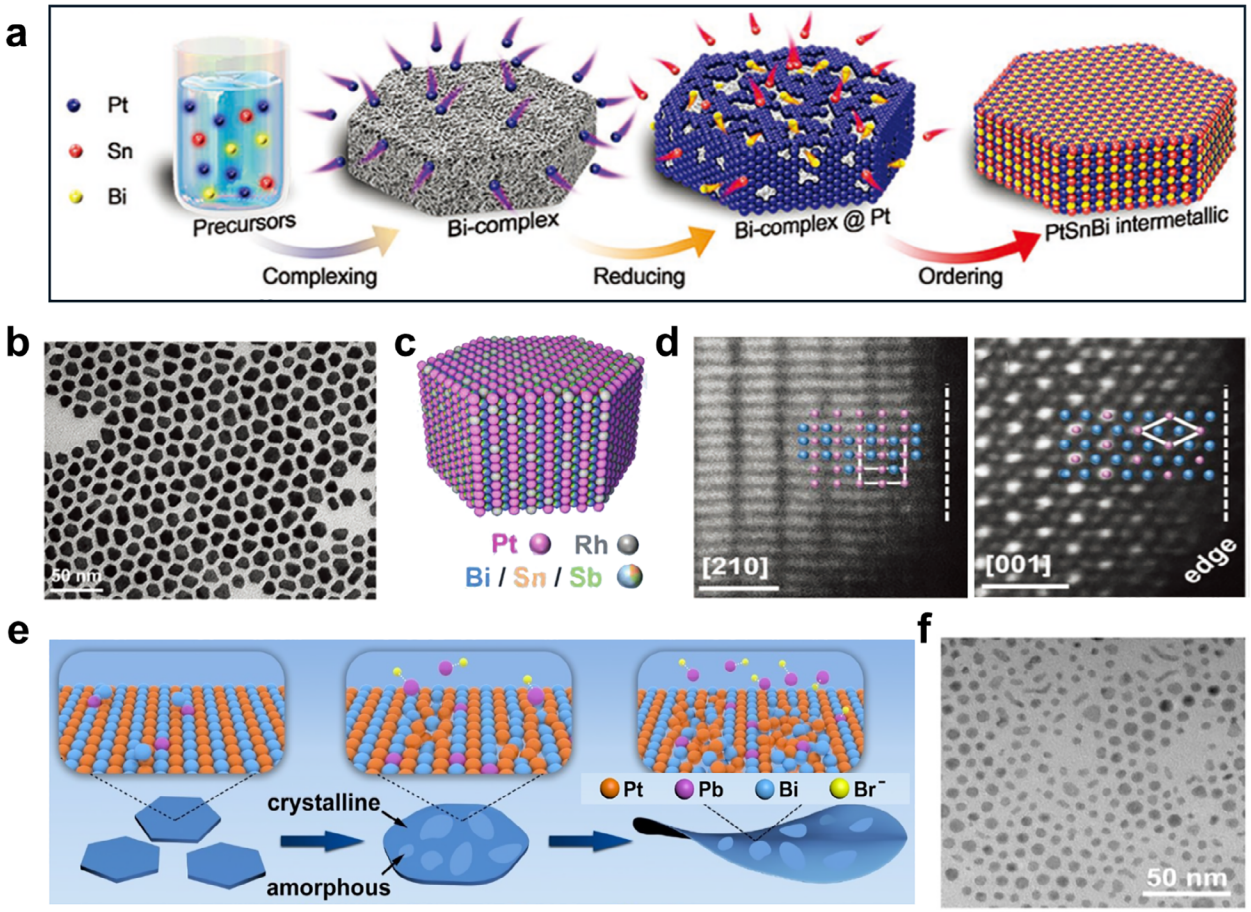

Figure 9. a) Schematic illustration of the synthesis of intermetallic $Pt_{45}Sn_{25}Bi_{30}$ nanoplates. b) TEM image. Reproduced with permission.[66] Copyright 2019, Wiley-VCH. c) Schematic diagram of the atomic arrangement of Pt/Rh/Bi/Sn/Sb atoms on the surface of the PtRhBiSnSb MCI nanoplate. d) HAADF-STEM images, the insets show the corresponding PtBi unit cells viewed along different zoom axes. Reproduced with permission.[55] Copyright 2022, Wiley-VCH. e) Schematic illustration of the PtPbBi nanosheet synthesis. f) TEM image of PtPbBi nanosheets. Reproduced with permission.[67] Copyright 2024, Wiley-VCH.

nanocrystals.[55,66–68] For instance, Quan et al. employed wet chemical techniques with a low temperature of 220 °C to produce ternary PtSnBi (**Figure 9**a,b)[66] and quinary PtRhBiSnSb MCIs (Figure 9c,d),[55] while Lu et al. synthesized PtPbBi intermetallic compounds using similar methods (Figure 9e,f).[67] Compared with the thermal annealing or Joule heating method, the wet chemistry method avoids high-temperature annealing, thereby preventing particle agglomeration during the annealing process. Although wet chemical methods enable the controlled synthesis of intermetallic nanocrystals with various morphologies, yielding specific highly active crystal facet catalysts characterized by uniform nanocrystal size. The complex kinetics and thermodynamics of the synthesis process result in poor reproducibility and present challenges for large-scale production. Moreover, these methods are limited in preparing MCIs with strongly immiscible elements, often leading to phase separation. Consequently, further exploration is required to develop strategies for directly obtaining MCIs via wet chemical methods. Wet chemistry synthesis methods enable the controlled fabrication of MCI nanocrystals with desired morphologies, which can increase their surface area and expose highly active crystal facets, enhancing catalytic performance. However, the intricate kinetics and thermodynamics involved in the process are not yet fully understood, resulting in issues with reproducibility and scalability. Additionally, the surfactants employed during synthesis tend to adhere strongly to the nanocrystal surfaces, complicating their subsequent removal. Therefore, further investigation is necessary to develop more effective strategies for the direct synthesis of MCI via wet chemistry routes.

3.4. Other Methods

Alternative synthesis methods include dealloying,[60] arc melting,[47] etc. Those methods are more scalable and straightforward but may lack the precise compositional and morphology control offered by approaches (see Sections 3.1, 3.2, and 3.3). The dealloying method, in general, displays a hierarchical nanoporous structure. For example, Liu et al. initially prepared $L1_2$-FeCoNiAlTi bulk alloys with a dual-phase structure.[60] Then they employed a one-step dealloying process to selectively remove one phase, yielding the MCI phase and resulting in a porous

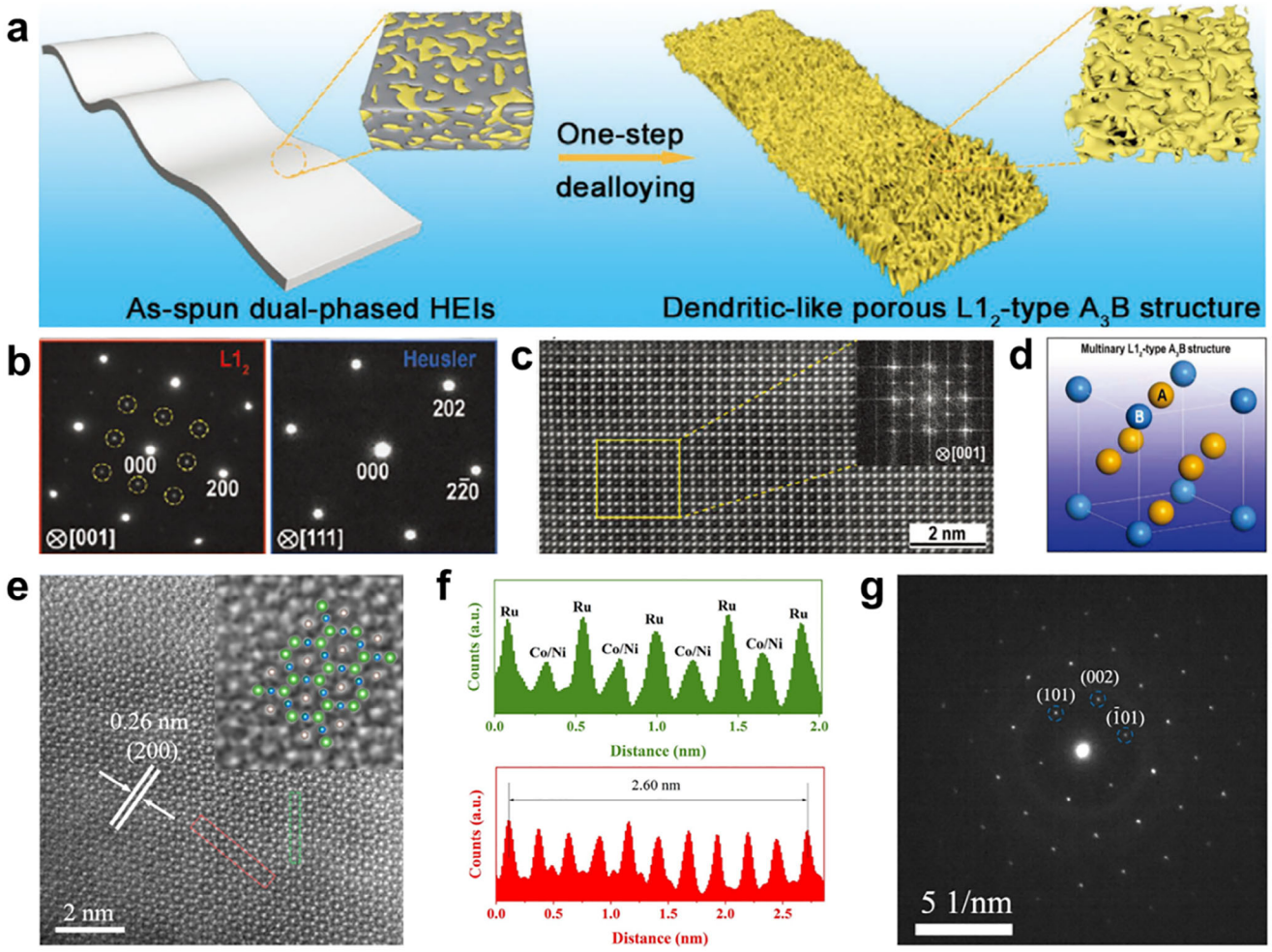

Figure 10. a) Schematic diagram of the dealloying process from a dual-phase structure to a $L1_2$-FeCoNiAlTi structure. b) TEM image with corresponding selected area electron diffraction (SAED) patterns showing the $L1_2$ and Heusler phases in the as-prepared MCI. c) Aberration-corrected HAADF-STEM image viewed along the [001] zone axis indicating the $L1_2$-type structure. The inset shows the corresponding SAED pattern. d) $L1_0$-FeCoNiAlTi DFT model (A: AlTi, B: FeCoNi). Reproduced with permission.[60] Copyright 2020, Wiley-VCH. e) HAADF-STEM image of $LaNi_{0.5}Co_{0.5}Ru$. The inset shows the crystal structure viewed along the [010] direction. f) The intensity profiles inside the red and green dashed boxes are derived from e). g) SAED pattern of $LaNi_{0.5}Co_{0.5}Ru$. Reproduced with permission.[47] Copyright 2020, Wiley-VCH.

structure (**Figure 10**a–d). Another alternative synthesis using arc melting for LaNiCoRu ingots fabricated by arc melting using various metal powders (Figure 10e–g).[47] This melting process was repeated 30 times to ensure compositional homogeneity. After cooling to room temperature, the material was crushed into powder to achieve the MCI nanocrystals. These preparation methods show considerable potential in the fabrication of MCI nanomaterials and are worth further exploration to develop the most efficient and convenient methods for MCI nanomaterial production.

4. Platinum Group Metals-Based MCIs and Non-Noble Metals-Based MCIs

4.1. Platinum Group Metals-Based MCIs

Platinum group metals (including Pt, Ru, Pd, Ir, Rh, and Os), situated in the 5*d*-block, exhibit distinct orbital hybridization behaviors when forming MCI nanocrystals with various elements, profoundly impacting the electronic structure and catalytic performance of these materials. In this section, we will discuss the multiple effects that arise when metals from different blocks (3*d*-block transition metals, *p*-block metals, and *f*-block rare earth metals) of the periodic table form MCIs with platinum group metals. For example, the hybridization of platinum group metals with 3*d*-block transition metals typically involves strong interactions between platinum group metals (5*d*) orbitals and the 3*d* orbitals of the transition metals, resulting in significant modifications to electron density and catalytic activity, particularly in electrocatalytic processes, such as ORR. This is discussed in more detail in Section 5.1. In contrast, the hybridization of platinum group metals with *p*-block metals generally involves mixing *s*/*p* orbitals with *d* orbitals, giving rise to unique electron donor-acceptor interactions that confer enhanced resistance to poisoning and improved catalytic activity. While platinum group metals hybridize with *f*-block metals, often

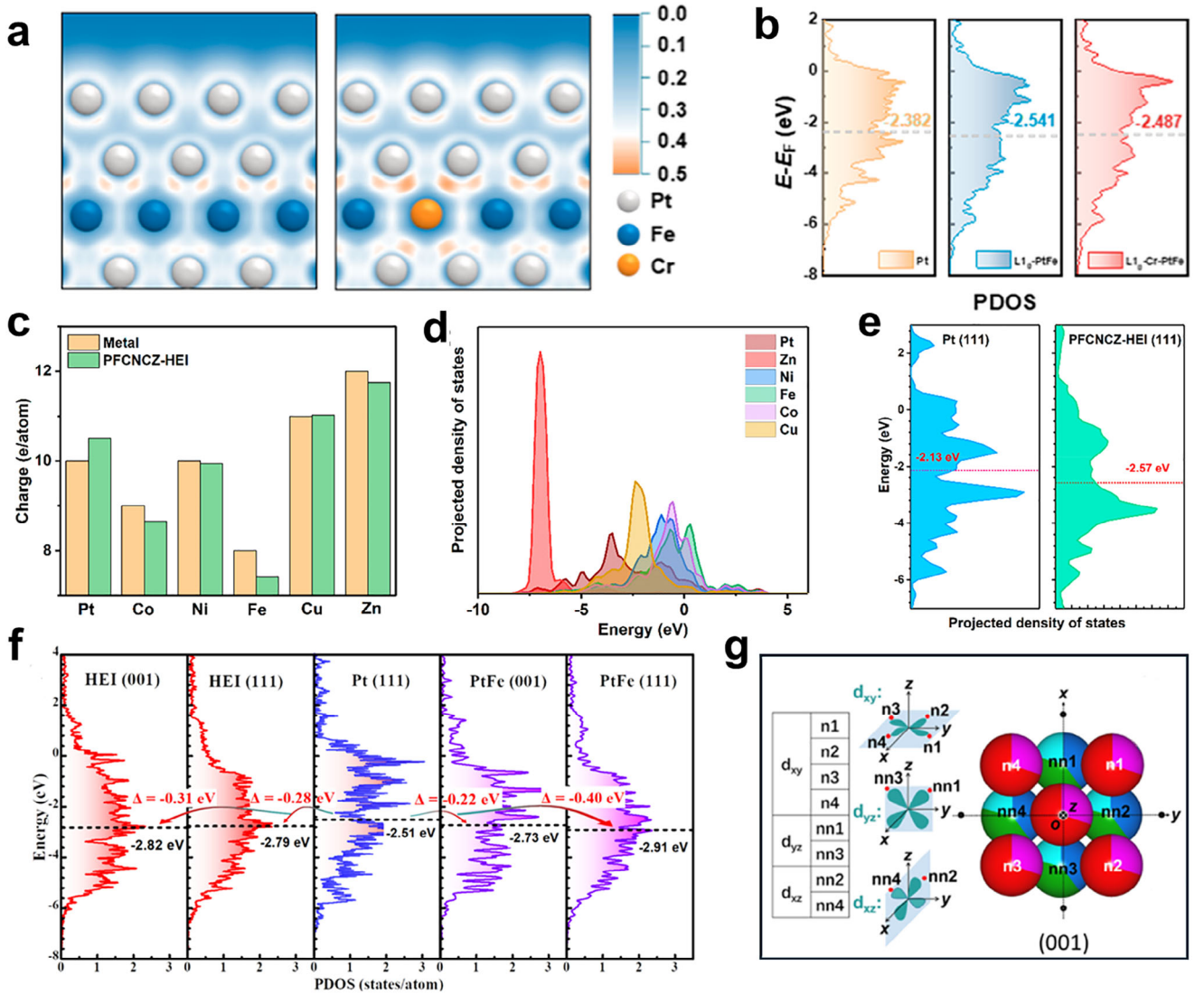

Figure 11. a) Sliced electron localization function for the $L1_0$-PtFe/Pt slab (left) and the $L1_0$-Cr-PtFe/Pt slab (right). b) *d*-band projected electronic densities of states (PDOS) for $L1_0$-Cr-PtFe/Pt, $L1_0$-PtFe/Pt, and pure Pt. Reproduced with permission.[78] Copyright 2024, American Chemical Society. c) The number of outermost *s* and *d* orbitals' electrons in the surface atoms of $L1_0$-Pt(FeCoNiCuZn)-MCI and the corresponding pure metal. d) PDOSs of surface Pt-*d*, Co-*d*, Ni-*d*, Cu-*d*, Zn-*d*, and Fe-*d* for $L1_0$-Pt(FeCoNiCuZn)-MCI. e) PDOSs of the Pt atom for Pt and $L1_0$-Pt(FeCoNiCuZn)-MCI. f) Electronic DOS of the *d*-band for the surface Pt atoms in the different nanomaterials. g) Spatial configurations of the nearest neighbors of the surface Pt in the $L1_0$-PtIr(FeCoCu)-MCI. Reproduced with permission.[111] Copyright 2023, American Chemical Society.

alongside 3*d* transition metals, the highly localized *f* orbital electrons result in relatively weak interactions. Nevertheless, multi-orbitals of the 5*d* orbital of platinum group metals, 4*d* orbital of *f*-block metals, and 3*d* transition metals usually impart distinctive properties to the resulting MCIs. Notably, the multi-orbital hybridization observed in these complex systems holds considerable potential for application in intricate electrocatalytic reactions.

4.1.1. Pt and 3d-Block Transition Metals

The hybridization between the partially filled *d* orbitals of 3*d* metals and the 5*d* orbitals of Pt is crucial in determining the catalytic behavior. Therefore, understanding the orbital hybridization in MCIs is crucial for designing high-performance electrocatalysts. Specifically, MCIs are predominantly synthesized through alloying Pt ([Xe] $4f^{14}$ $5d^{9}$ $6s^{1}$) with 3*d* transition metals (M, $3d^{1-10}$ $4s^{1\sim2}$) such as Cr ([Ar] $3d^{5}$ $4s^{1}$), Mn ([Ar] $3d^{5}$ $4s^{2}$), Fe ([Ar] $3d^{6}$ $4s^{2}$), Co ([Ar] $3d^{7}$ $4s^{2}$), Ni ([Ar] $3d^{9}$ $4s^{1}$), and Cu ([Ar] $3d^{10}$ $4s^{1}$), forming $Pt_m(M_1M_2...)_n$ MCIs. In these systems, the interaction between Pt(5*d*) and M(3*d*) orbitals modifies the Pt(5*d*) band structure, leading to changes in Pt-Pt atomic distances and coordination numbers. This orbital interplay causes the *d*-band center of Pt to shift downward relative to the Fermi level, which alters electronic structure of Pt by introducing ligand effects that impact electrocatalyst activity and stability. Moreover, the inherent complexity of MCIs results in strain effects. Noteworthy investigations by Wang

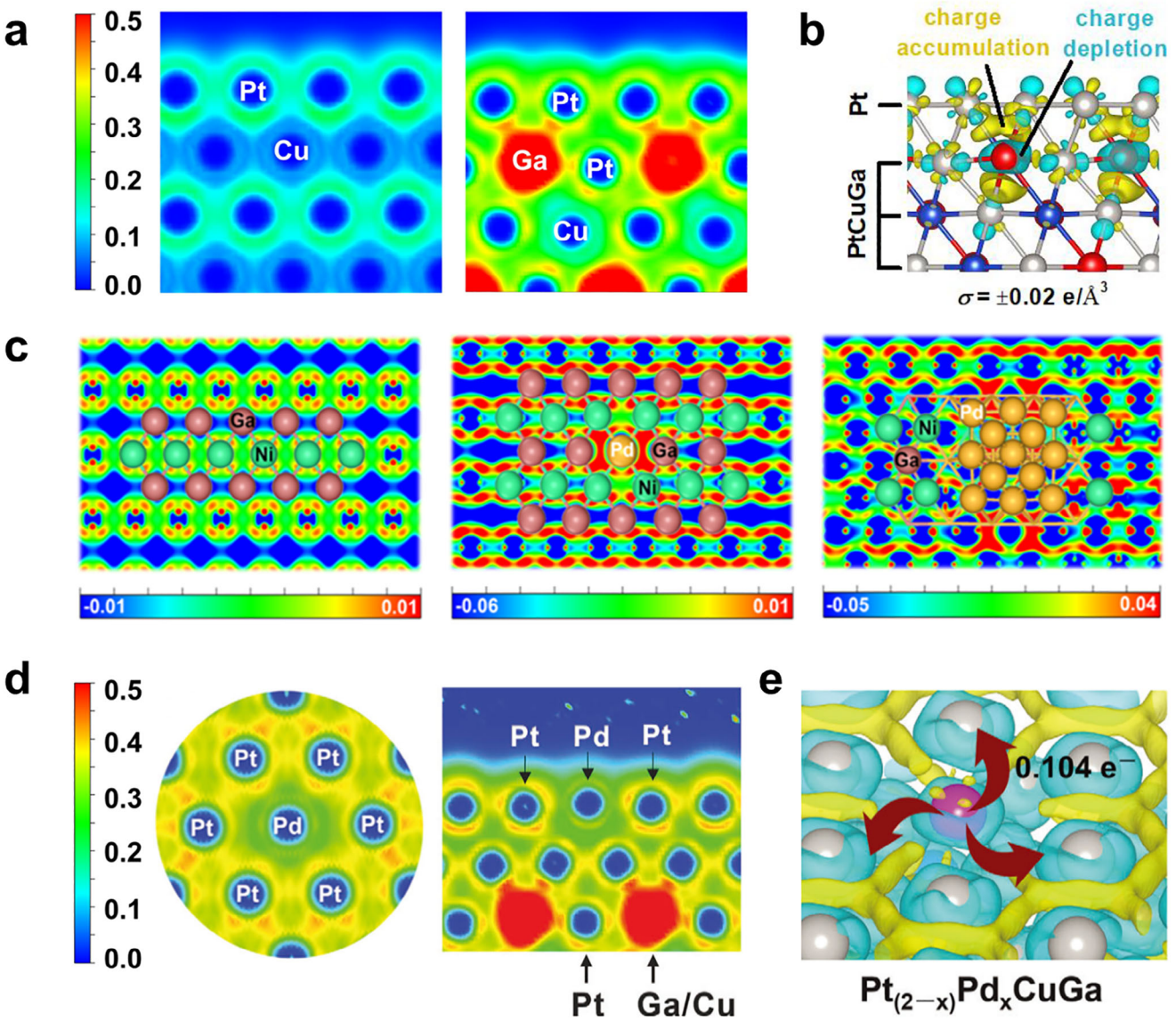

Figure 12. a) Sliced electron localization function for $L1_1$-PtCu/Pt slab and $L1_0$- Pt_2CuGa/Pt. b) Differential charge density iso-surfaces induced by the introduction of Ga into the PtCu structure. Reproduced with permission.[53] Copyright 2023, Wiley-VCH. c) Charge density difference of NiGa (110), Pd_1-NiGa (110), and Pd_n-NiGa (110) surfaces. Reproduced with permission.[71] Copyright 2024, Wiley-VCH. d) Sliced electron localization function. e) Charge density of $Pt_{2-x}Pd_xCuGa$ (111). Reproduced with permission.[54] Copyright 2024, Wiley-VCH.

et al. have explored ternary alloys such as PtCoNi,[63] PtFeCu,[64] PdZnAu,[79] PtPdFe,[65] and PtRhFe,[62] alongside quinary MCIs like $L1_2$-Pt(FeCoNiCuZn)$_3$[108] and (PtPdIrRu)$_2$FeCu.[35] Liang et al. have studied MCIs including Pt_2CoCu, $Pt_3FeCoNi$, $Pt_4FeCoNiCu$, $Pt_5FeCoNiCuMn$,[33] Pt_2CoCu/Pt_2CoNi,[110] and Pt(FeCoNiCu)$_3$.[44] Their study reveals that MCIs display ligand, geometric, and strain effects (either individually or in synergy) that collectively enhance electrocatalytic activity.

Li et al. explored the strain effects and ligand effects synergistic combination in MCI nanocrystals.[78] They introduced Cr into $L1_0$-PtFe (**Figure 11a**), resulting in a strain effect due to the larger atomic radius of Cr, which caused an upward shift in the *d*-band center of $L1_0$-Cr-PtFe (−2.487 eV, Figure 11b). Cr incorporation induces a ligand effect that accelerates electron migration from the bulk to the surface. Moreover, the concomitant changes in the electronic structure markedly enhance the stability of $L1_0$-Cr-PtFe, notably stabilizing Fe atoms within the lattice. This effect arises from the strong Fe—Cr interactions and the spatial constraints on Fe diffusion imposed by the larger atomic radius of Cr, with the enhanced 5d-3d interactions between Pt and Fe further contributing to the stabilization. Furthermore, Xia et al. observed charge transfer between the outermost *s* and *d* orbitals of surface metal atoms in $L1_0$-Pt(FeCoNiCuZn) MCI nanocrystals (Figure 11c).[36] They found that ligand effects cause electron transfer from M (Fe, Co, Ni, and Cu) to Pt, reducing the outer layer electrons of Fe, Zn, Co, and Ni, while increasing those of Pt. Significant broadening of the *d*-band electron orbitals enhances orbital overlap and charge transfer between

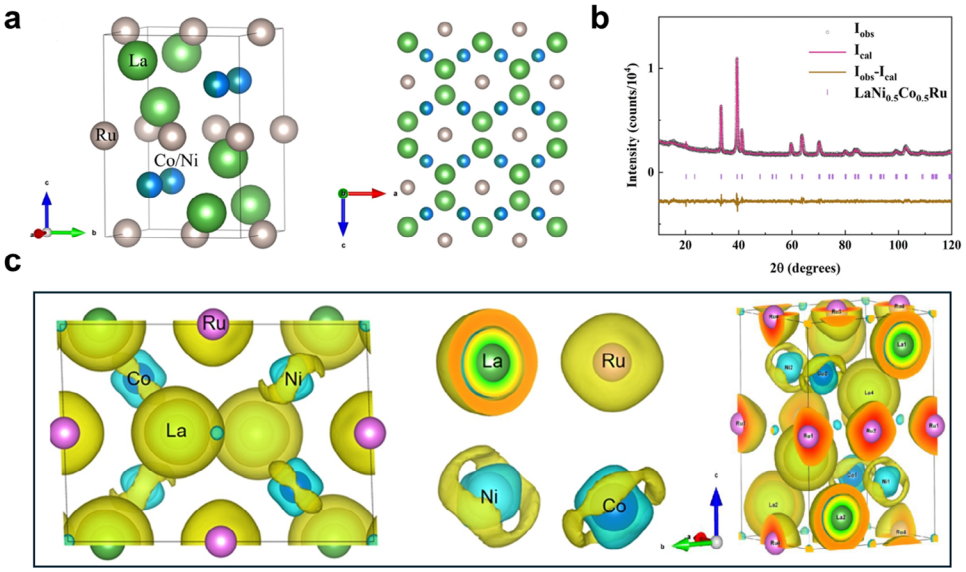

Figure 13. a) The $LaNi_{0.5}Co_{0.5}Ru$ lattice structures are viewed from different perspectives. b) X-ray diffraction patterns. c) The 3D view of deformation density maps of the bulk $LaNi_{0.5}Co_{0.5}Ru$. Electron accumulation and depletion are shown by the yellow and cyan regions, respectively. Reproduced with permission.[47] Copyright 2024, Wiley-VCH.

different metals (Figure 11d,e). This strong bonding interaction further stabilizes the MCI structure. The same research group also investigated the intricate electronic interactions in MCIs, revealing complementary insights into their catalytic activity and stability.[111] They synthesized the $L1_0$-PtIr(FeCoCu) MCIs and identified electron density transfer from M (M=Fe, Co, Cu) to Pt/Ir atoms (Figure 11f). This electron transfer optimizes the electronic structure of Pt, resulting in a downward shift in its *d*-band center. This effect is more pronounced on the MCI (001) surface, where d_{yx}, d_{yz}, and d_{xz} orbitals directly interact with surrounding metal atoms, allowing the electronic structure of Pt to be finely tuned by Fe, Co, Cu, and Ir (Figure 11g). This high activity on low-index crystal planes (001) likely arises from the synergistic ligand and strain effects in MCIs.

Current research on Pt and 3*d* transition metal-formed MCIs has significantly advanced in understanding the ligand and strain effects, yet several challenges remain. The development has predominantly focused on a limited range of *d*-band metals such as Fe, Co, Ni, Cu, and Mn, leaving potentially valuable materials unexplored. Additionally, a comprehensive understanding of electronic structures and the ability to predict and control performance in practical applications are still lacking.

4.1.2. Pt and p-Block Element (Ga, In, or Sn)

Those metals in the *p*-block are filling *p* orbitals. Their general electronic configuration is ns^2 np^{1-6}. Pt and *p*-block low-melting metals, such as Ga, In, and Sn, can induce localized electronic structure through *p-d* orbital coupling between Pt(5*d*) and low-melting-point metal (4*p*) to enhance covalent bonding and achieve highly stable structure. For example, Liang et al. prepared $L1_0$-PtGaNi/PtGaFe,[50] and low-melting-point metal (Ga, Cd, and Sb) doped-Pt_5Ce,[51] achieved the regulation of bonding structure. Similarly, Li et al. reported that $L1_0$-Pt_2CuGa nanocrystals exhibit enhanced catalytic performance due to directional covalent bonds induced by *p-d* orbital hybridization (**Figure 12a**).[53] Incorporation of Ga into PtCu induces the formation of Pt-Ga covalent bonds concomitant with a phase transition from the $L1_1$ to the $L1_0$ structure. This transformation results in a reduced Pt valence state and facilitates substantial electron transfer between Ga and Pt. Charge accumulation between subsurface Ga and adjacent Pt atoms corroborates the formation of these covalent bonds in $L1_0$-Pt_2CuGa-a feature absent in PtCu or CuGa (Figure 12b). The robust Pt-Ga interaction can be ascribed to the elevated *p*-band center of Ga, which shifts the *p-d* antibonding state upward, thereby reinforcing the covalent bond. Duan et al. reported that in $Pd_1Ni_2Ga_1$, Pd atoms acquire a negative charge as a consequence of electron transfer from neighboring Ni and Ga atoms (Figure 12c).[71] Significant hybridization among the Ni 3*d*, Pd 4*d*, and Ga 4*p* orbitals drives electron transfer sequentially from Ga to Ni and subsequently from Ni to Pd. Furthermore, the concomitant upward shift of the Ni *d*-band center and downward shift of the Pd *d*-band center in $Pd_1Ni_2Ga_1$ underscore the pronounced influence of the Pd_1-NiGa catalyst on adsorbate regulation. Liu et al. similarly demonstrated that the addition of Ga to PtCu intermetallic compounds induces a structural transformation from $L1_1$ to $L1_0$, yielding directional Pt-Ga covalent bonds via *p-d* orbital hybridization (Figure 12d).[54] Moreover, the strain effect was found to effectively augment orbital hybridization; incorporation of Pd into the $Pt_{2-x}Pd_xCuGa$ lattice engenders compressive strain, thereby enhancing orbital overlap between Pt and adjacent metal atoms. Consequently, electron density redistributes, accumulating around surface Pt atoms while delocalizing near Pd atoms (Figure 12e). Such electron enrichment at Pd sites is advantageous for the adsorption of electron-rich species. Collectively, these findings underscore the pivotal role of Pt 5*d*-*p*-block (4*p*) orbital hybridization in modulating the electronic structure and electrocatalytic

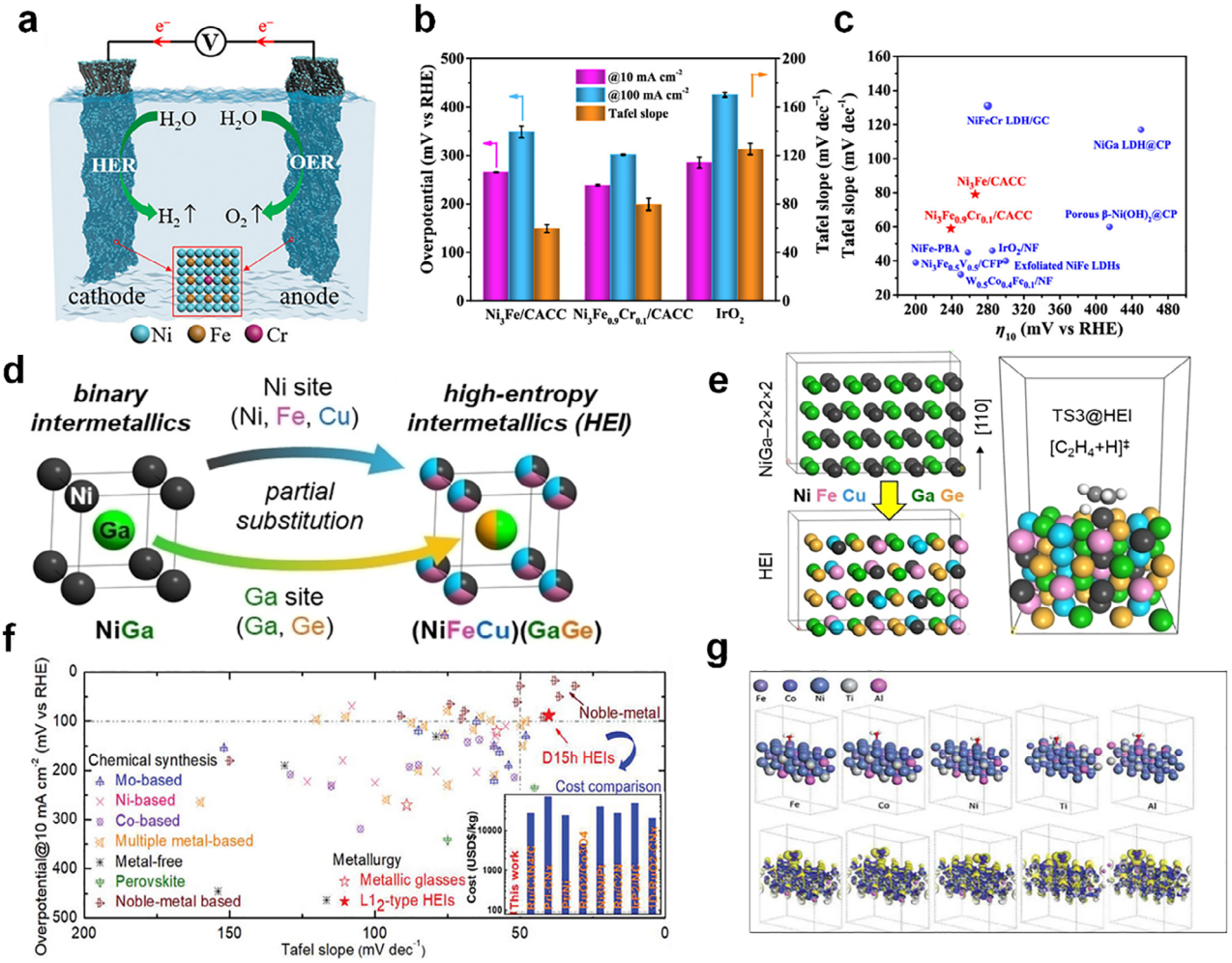

Figure 14. a) schematic for application of $Ni_3Fe_{1-x}Cr_x$ intermetallic integrated electrodes. b) Comparison of the OER overpotentials at 10 and 100 mA cm^{-2} and the Tafel slopes. c) Comparison of the overpotentials at 10 mA cm^{-2} and the Tafel slopes with the recently reported catalysts. Reproduced with permission.[81] Copyright 2022, American Chemical Society. d) NiGa to (NiFeCu)(GaGe) MCI. e) The MCI model and an example of hydrogen attack to C_2H_2 on MCI. Reproduced with permission.[72] Copyright 2022, Wiley-VCH. f) Comparison of overpotentials at 10 mA cm^{-2} versus Tafel slopes. g) DFT simulations of atomic configurations and the corresponding electron density difference at the $L1_2$ MCI-(100) surface after H_2O adsorption at different element sites. Reproduced with permission.[60] Copyright 2020, Wiley-VCH.

performance of MCI nanocrystals. In conclusion, the capacity to engineer directional covalent bonds and tailor electronic states via phase transitions and *p-d* orbital hybridization presents promising avenues for the rational design of high-performance catalysts.

4.1.3. Ru and f-Block Element

The coupling between platinum group metals, *f*-block metals, and other metals through multiple *d* orbitals generates synergistic effects (e.g., 5*d*-4*d*-3*d*). This interaction holds significant promise for advancing electrocatalysis applications. For instance, Zhong et al. synthesized MCIs of platinum group metal Ru and *f*-block elements (La), specifically $RuLaNi_{1-x}Co_x$, which contain 5*d*, 4*d*, and 3*d* electrons.[47] The study reveals a synergistic interplay among 5*d*, 4*d*, and 3*d* electron orbitals in these MCIs (**Figure 13**a,b). Notably, the 5*d* orbital of La ($[Xe]5d^16s^2$) donates electrons to the 4d orbital of Ru, resulting in negative valence states for both Ru and Ni/Co-a manifestation of pronounced electron-donating capacity of La. Quantitative topological analysis and deformation density mapping of $LaNi_{0.5}Co_{0.5}Ru$ (Figure 13c) further elucidate this interatomic coupling: the 5*d* orbital of La exhibits electron depletion (inner cyan area) while an electron-rich domain forms in its periphery (outer yellow area), concomitant with electron accumulation in Ru 4*d* orbital. Moreover, the 3*d* orbitals of Ni/Co interact with La 5*d* and Ru 4*d* orbitals, giving rise to an inner electron-deficient region with a distinct orientation and an outer annular electron-rich region. These findings underscore the critical role of synergistic *d*-orbital coupling among platinum-group metals, *f*-block metals, and 3*d* transition metals in modulating the electronic properties of MCIs.

Platinum group metals and *f*-block metals often exhibit complex multi-orbital hybridization, challenging their structural

Table 1. Summary of MCIs for electrocatalysis synthesis and applications.

MCI Catalysts	Structure	Synthetic methods	Applications	Performance	Stability	Refs.
$Pt(FeCoNiCuZn)_3$	$L1_2$	Thermal annealing	ORR	$E_{1/2}$[a] = 0.922 V	30, 000 cycles	[108]
Au-O-PdZn	$L1_0$	Thermal annealing	ORR	$E_{1/2}$ = 50 V	30, 000 cycles	[79]
Pt_2CoCu/Pt_2CoNi	$L1_0$	Thermal annealing	ORR	MA[b] ≈3.0 A mg^{-1}_{Pt} SA[c] = 3.5 mA cm^{-2}	30 K cycles	[47]
Pt_2CoCu, $Pt_3FeCoNi$ $Pt_4FeCoNiCu$ $Pt_5FeCoNiCuMn$	$L1_0$	Thermal annealing	ORR	MA = 4.18 mg^{-1}_{Pt} SA = 3.8 mA cm^{-2}_{Pt}	30, 000 cycles	[33]
Ga-PtNi/Ga-PtFe	$L1_0$	Thermal annealing	ORR	MA = 1.07 A mg^{-1}_{Pt} SA = 4.74 ±0.16 mA cm^{-2}_{Pt}	100 h	[50]
$Pt(FeCoNiCu)_3$	$L1_2$	Thermal annealing	ORR	MA = 2.71±0.11 A mg^{-1}_{Pt} SA = 3.82 mA cm^{-2}	30000 cycles	[44]
M-Pt_5Ce (M = Ga,Cd, and Sb)	$D2_d$	Thermal annealing	ORR	$E_{1/2}$≈0.910–0.927 V	30000 ADT cycles	[51]
$Pt_{50}Ni_{35}Ga_{15}$	$L1_0$	Thermal annealing	ORR	MA = 1.98 A $mgPt^{-1}$ SA = 2.96 mA cm^{-2}	3, 000 cycles	[52]
Pt_2CuGa	$L1_0$	Thermal annealing	ORR	$E_{1/2}$ = 0.936 V vs RHE MA = 1.39 A mg^{-1}_{Pt} SA = 2.86 mA cm^{-2}	30, 000 cycles	[53]
Cr-PtFe	$L1_0$	Thermal annealing	ORR	$E_{1/2}$ = 0.952 V vs RHE MA = 2.05 A Mg^{-1}_{Pt} SA = 3.55 mA cm^{-2}	30000 ADT cycles	[78]
PtCoTi	$L1_2$	Thermal annealing	ORR	$E_{1/2}$ = 0.94 V Tafel slope = 53 mV dec^{-1}	20000 cycles	[58]
PtFeCoNiCuZn	$L1_0$	Thermal annealing	ORR	$E_{1/2}$ = 0.9406 V Tafle slope = 59 mV dec^{-1}	10000 cycles	[36]
PtIrFeCoCu	$L1_0$	Thermal annealing	ORR	$E_{1/2}$ = 0.894 V Tafle slope = 63.5 mV dec^{-1}	60000 cycles	[111]
PdFeCoNiCu	$L1_0$	Thermal annealing	ORR	$E_{1/2}$ = 0.90 V Tafel slope = 55 mV dec^{-1}	10000 cycles	[57]
PtFeCu	$L1_0$	Thermal annealing	ORR	$E_{1/2}$ = 0.955 V	20000 cycles	[56]
PtZnCu	$L1_0$	Thermal annealing	ORR	$E_{1/2}$ = 0.93 V vs RHE	10000 cycles	[75]
(Fe,Co,Ni)/Pt	$L1_0$	Thermal annealing	ORR	$E_{1/2}$ = 0.92 V vs RHE	50000 cycles	[73]
PtCoNi	$L1_2$	Thermal annealing	ORR	$E_{1/2=}$ 0.941 V vs RHE E_{onset}[a] = 0.1 mA m^{-2} Tafel slope = 73.1 mV dec^{-1}	30000 cycles	[76]
PtCoMn	$L1_0$	Thermal annealing	ORR	$E_{1/2}$ = 0.940 V vs RHE Tafel slope = 56.42 mv dec^{-1}	30000 ADT cycles	[80]
$Pt_4FeCoNiCu$	$L1_0$	Thermal annealing	ORR	$E_{1/2}$ = 0.930 V	20000 ADT cycles	[46]
$Pt_4FeCoCuNi$	$L1_0$	Thermal annealing	ORR	$E_{1/2}$ = 0.943 V Tafel slope = 51.5 mv dec^{-1}	30000 cycles	[45]
PtPdFeCoNi	$L1_0$	Thermal annealing	ORR	$E_{1/2}$ = 0.91V Tafel slope = 60.2 mV dec^{-1}	50 000 cycles	[59]
$LaNi_{1-x}Co_xRu$	$D1_b$	Thermal annealing	HER	Tafel slope = 70 mv dec^{-1}	50 h	[47]
FeMnPt	$L1_0$	Thermal annealing	HER	Tafel slope≈30 mV dec^{-1}	12∼15 h	[74]
PtCuPdAgFe	$L1_0$	Thermal annealing	HER	Tafel slope = 29 mV dec^{-1}	10000 cycles	[61]
FeCoNiAlTie	$L1_2$	Dealloying	HER	Tafel slope = 40.1 mV dec^{-1}	40 h	[60]
$Pt_4FeCoCuNi$	$L1_0$	Thermal annealing	HER	Tafel slope = 31 mV dec^{-1}	50 h	[45]
PtSnBi	$L1_0$	Wet chemistry	FAOR	MA = 4.394 A mg^{-1}_{Pt}	4000 cycles	[66]
$(PtPdIrRu)_2$ FeCu	$L1_0$	Thermal annealing	FAOR	MA≈0.30A mg^{-1}_{PGM} SA≈1.83 mA cm^{-2}_{PGM}	1200 cycles	[35]
PtCoNi	$L1_0$	Thermal annealing	FAOR	E_{onset}≈0.25 V vs RHE	10000 s	[63]
RhPtFe	$L1_0$	Thermal annealing	FAOR	E_{onset}≈0.12 V vs RHE	100 cycles	[62]

(*Continued*)

Table 1. (Continued)

MCI Catalysts	Structure	Synthetic methods	Applications	Performance	Stability	Refs.
CuPtSn	$L1_2$	Wet chemistry	MOR	E_{onset} ≈0.45V vs RHE Tafel slope = 223.7 mV dec^{-1}	1500 cycles	[68]
PtPbBi	$L1_0$	Wet chemistry	MOR	E_{onset} ≈0.4 V vs RHE Tafel slope = 20 mV dec^{-1}	100 h	[67]
PtRhBiSnSb	$L1_0$	Wet chemistry	MOR	E_{onset}: 0.1 V vs RHE lower than Pt/C	5000 cycles	[55]
PtSnMn	$L1_2$	Thermal annealing	MOR	E_{onset} = 0.089 V vs Ag/AgCl	3600 s	[70]
PtRhFe	$L1_2$	Thermal annealing	MOR	E_{onset} = −0.48 V	500 cycles	[69]
PtPdCuGa	$L1_0$	Thermal annealing	MOR	E_{onset} = 0.508 V vs. RHE@0.5 mA $cm^{-2}{}_{PGM}$ Tafel slope = 127 mV dec^{-1}	20–30 cycles	[54]

[a] $E_{1/2}$ = Half-wave potential, and E_{onset} = Onset potential; [b] Mass activities; [c] Specific activities.

analysis in MCIs and necessitating multi-scale characterization techniques. Additionally, platinum group metals-*f* block metals MCI nanocrystals, such as those alloyed with Y or Er, show great promise as highly active and selective catalysts. Investigating these relatively unexplored MCI nanocrystals could reveal their significant potential and lead to central catalysis and materials science advancements.

4.2. Non-Noble Metal-Based MCIs

In addition to Pt-based MCI nanocrystals, recent advances in non-noble metal MCI have demonstrated remarkable catalytic performance across diverse energy conversion applications, driven by their unique atomic ordering and synergistic elemental interactions. A notable example is the $Ni_3Fe_{0.9}Cr_{0.1}$ intermetallic electrode synthesized via ultrafast carbothermal shock,[81] which exhibits exceptional bifunctional activity for overall water splitting (**Figure 14a**). The ordered $L1_2$-type structure facilitates Cr substitution at Fe sites, promoting the formation of OER-active Ni^{3+}/Fe^{3+} species while reducing the energy barrier for water dissociation. This structural precision enhances both HER (128 mV@10 mA cm^{-2}) and OER (239 mV@10 mA cm^{-2}) activities, rivaling noble-metal benchmarks (Figure 14b,c). Companion to HEAs with comparable compositions (e.g., CrMnFeNi) rely on phase engineering and surface reconstruction to enhance catalytic activity,[112] this $Ni_3Fe_{0.9}Cr_{0.1}$ intermetallic work underscores how site-specific substitution in intermetallics optimizes electronic configurations and surface dynamics.

Expanding this concept to multicomponent systems, Ma et al.[72] engineered a B2 type NiFeCuGaGe MCI for acetylene semihydrogenation. By partially replacing Ni with Fe/Cu and Ga with Ge, the MCI achieves atomic isolation of active Ni sites within a chemically ordered framework (Figure 14d). This design not only suppresses ethylene overhydrogenation at full acetylene conversion but also delivers a fivefold activity enhancement over conventional Ni-based catalysts. DFT studies reveal that surface energy reduction and weakened ethylene adsorption stem from the synergistic interplay of multimetallic sites (Figure 14e). To further amplify structural complexity while maintaining atomic-level control, Jia et al.[60] developed an $L1_2$ -type FeCoNiAlTi MCI with dendritic porosity for alkaline HER. The ordered sublattice arrangement-Al/Ti at vertices and Fe/Co/Ni at face centers-creates site-isolated active regions. A comprehensive comparative analysis of overpotential and Tafel slope characteristics among approximately 60 distinct HER electrocatalysts was conducted under alkaline conditions (1.0 M KOH) at a current density of 10 mA cm^{-2}. The experimental results demonstrated that $L1_2$ MCI exhibits remarkable electrocatalytic performance, serving as a cost-effective alternative to precious metal-based catalysts in hydrogen evolution reactions (Figure 14f). Theoretical calculations attribute this to Ti-mediated H_2O adsorption and optimized H* binding energies at Fe/Co/Ni sites coordinated with Al, illustrating how chemical complexity and crystallographic order jointly regulate reaction pathways (Figure 14 g). These studies collectively highlight the catalytic potential of non-noble metal MCIs, taking advantage of atomic-level ordering and multimetallic synergy to precisely tailor electronic structures and surface reactivity.

5. Electrocatalytic Applications of MCIs

MCI nanocrystals have emerged as promising candidates in the field of electrocatalysis due to their distinctive ordered superlattice structures and high-entropy effects within the sublattices. These unique properties enable the precise tuning of electronic characteristics and surface properties, essential for enhancing catalytic activity, selectivity, and stability.[113] Moreover, the complex atomic arrangements in MCIs generate diverse active sites, which facilitate the efficient adsorption, activation, and conversion of various molecules. Consequently, MCIs are highly versatile electrocatalysts that can effectively meet the challenges of sustainable energy conversion, including ORR, HER, FAOR, MOR, and others. Recent breakthroughs in MCI nanocrystal electrocatalysis have demonstrated their potential to break traditional activity-stability trade-offs and achieve unprecedented catalytic efficiencies (**Table 1**), marking a significant step forward in developing next-generation energy technologies.

5.1. ORR

ORR is a crucial reaction in energy conversion technologies, such as fuel cells and metal-air batteries, where efficient and stable

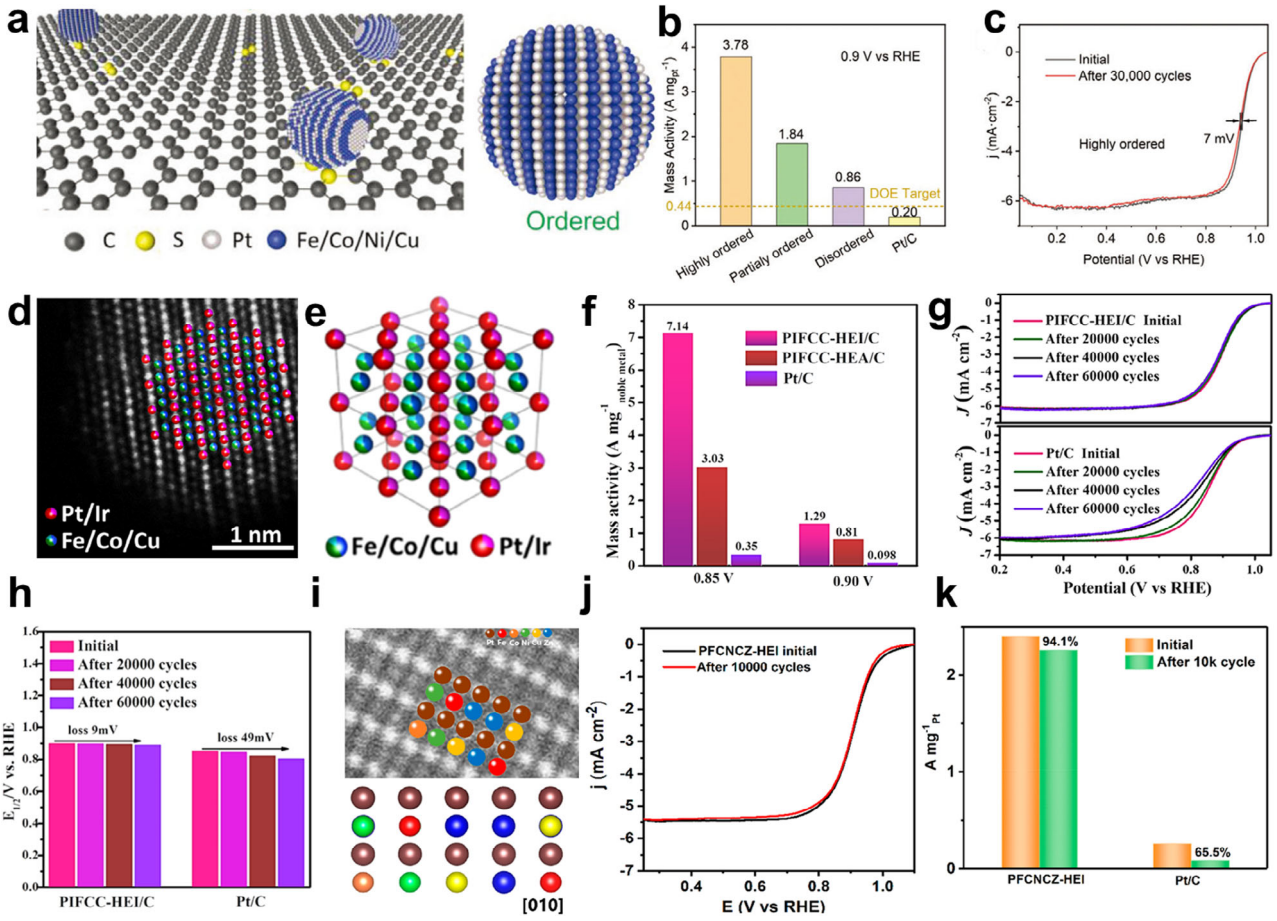

Figure 15. a) Schematic illustration of the synthesis process and a fully ordered Pt_4(FeCoCuNi) nanocrystal. b) Comparison of the mass activities. c) Stability test of the highly ordered Pt_4(FeCoCuNi) catalysts. Reproduced with permission.[45] Copyright 2023, Wiley-VCH. d) Atomically resolved HAADF-STEM image of an $L1_0$-PtIr(FeCoCu) MCI nanocrystals. e) Lattice diagram. f) Mass activity comparisons of $L1_0$-PtIr(FeCoCu)/C and commercial Pt/C. g) Stability test of $L1_0$-PtIr(FeCoCu) MCI nanocrystals and commercial Pt/C. h) Quantitative comparisons of the $E_{1/2}$. (i) Local structure image of MCI. Reproduced with permission.[111] Copyright 2023, American Chemical Society. j) Stability test of the $L1_0$-PtIr(FeCoCu) MCI nanocrystals. k) Mass activity before and after ADTs. Reproduced with permission.[36] Copyright 2023, American Chemical Society.

electrocatalysts are needed to overcome the sluggish kinetics of the reaction. MCI nanocrystals have shown exceptional promise due to their ability to fine-tune active sites and optimize electrocatalytic performance. As discussed in Section 4, multi-element electronic orbital hybridization plays a crucial role in modulating the electrocatalytic activity and stability of the ORR. The vital multiple orbital interaction potential is attributed to the stability of the ORR. Most importantly, by precisely tuning the orbital hybridization to optimize the *d*-band center, MCI nanocrystals can achieve an optimal balance between adsorption strength and desorption ease, enhancing the ORR kinetics. A *d*-band center that is neither too high nor too low ensures that reactants such as oxygen are sufficiently adsorbed to facilitate bond cleavage, while products such as water are readily desorbed from the catalyst surface.

Besides regulating orbital hybridization, the degree of ordering,[45] high-activity facets,[111] and size control are crucial for tuning the *d*-band center to boost ORR performance. For instance, Huang and coworkers have reported the effects of the degree of chemical ordering of $L1_0$-Pt_4(FeCoCuNi) MCI on electrocatalytic performance (**Figure 15a**).[45] The ordering degree of MCIs is precisely controlled by changing the annealing temperature and duration. Aberration-corrected HAADF-STEM was used to investigate the atomic-scale ordering transformation pathway and crystal transformation mechanism of $L1_0$-Pt_4(FeCoCuNi) with an average particle size of ≈5 nm. The characterization results demonstrate a downshift of the *d*-band center relative to Pt, leading to a favorable weakening of intermediate adsorption during ORR. Specifically, as for acidic ORR performance, ORR polarization curves of different catalyst samples for highly ordered $L1_0$-Pt_4FeCoCuNi showed a large half-wave potential ($E_{1/2}$), outperforming the partially ordered and disordered counterparts. Additionally, all the $L1_0$-Pt_4(FeCoCuNi) electrocatalysts showed higher $E_{1/2}$ than commercial Pt/C, demonstrating optimized ORR performance. Furthermore, highly ordered $L1_0$-Pt_4(FeCoCuNi) delivered the most significant mass activity (Figure 15b). Based on the above analysis, the higher degree of ordering contributed to higher ORR performance. Insights from the ORR polarization curves before and after 30000 cycles in acid via accelerated durability testing (ADT) between 0.5

and 1.1 V, the highly ordered Pt_4(FeCoCuNi) demonstrated the lowest negatively shift of $E_{1/2}$ (Figure 15c), when compared with partially ordered, disordered counterparts, and commercial Pt/C. Excellent catalytic activity and outstanding durability of highly ordered electrocatalysts for ORR could be ascribed to the entropy increment and ordered intermetallic structure.

Apart from the degree of chemical ordering regulation, constructing high-activity facets is essential to promote catalytic activity. Xia's group proposed a significant strategy to convert low-index facets into high-activity facets.[111] The structurally ordered $L1_0$-PtIr(FeCoCu) MCIs with an average diameter of 6 nm exhibited ultrahigh active facets (Figure 15d,e). As a result, the $L1_0$-PtIr(FeCoCu) MCI electrocatalyst for ORR achieves a much higher $E_{1/2}$ (0.9 V vs. RHE), an ultrahigh mass activity (7.14 A $mg_{noble\ metal}^{-1}$ at 0.85 V), and extraordinary durability over 60000 potential cycles (Figure 15f–h). Besides, the fuel cell assembled with $L1_0$-PtIr(FeCoCu) MCI nanocrystals delivered an ultrahigh peak power density of 1.73 W cm^{-2} at a back pressure of 1.0 bar without working voltage decay after 80 h, suggesting the top-level performance among reported fuel cells. The remarkable performance of $L1_0$-PtIr(FeCoCu) for ORR and fuel cells is mainly attributed to its ultrahigh active facets (001), the (001) facet (Figure 15i) affording the lowest activation barriers for the rate-limiting step ($OH^* + H^+ + e^- \rightarrow H_2O$), optimal *d*-band centers, and electron structure.

Additionally, size control of the MCI nanocrystals is also crucial for ORR performance. Previous literature has claimed that catalysts of 2–3 nm can achieve the highest mass activity and catalytic performance. Xia and coworkers had taken the space-confined strategy to fabricate ultrasmall and well-ordered $L1_0$-Pt(FeCoNiCuZn) MCI nanocrystals.[36] Acted as cathode for ORR (Figure 15j), $L1_0$-Pt(FeCoNiCuZn)- MCI demonstrated a higher $E_{1/2}$ (up to 0.906 V) than commercial Pt/C (0.862 V) and Pt(FeCoNiCuZn) HEA nanocrystals (0.878 V). Furthermore, the MCI nanocrystals exhibited an ultrahigh mass activity of 2.403 A mg_{Pt}^{-1} at 0.90 V versus RHE (Figure 15k), 19 times higher than that of commercial Pt/C. The proton-exchange membrane fuel cell assembled with $L1_0$-Pt(FeCoNiCuZn) MCI nanocrystals as cathode (0.03 mg_{Pt} cm^{-2}) showed a power density of 1.4 W cm^{-2}. ADTs performed in 0.1 M $HClO_4$, $L1_0$-Pt(FeCoNiCuZn) MCI nanocrystals displayed a slightly negligible $E_{1/2}$ degradation of only 1 mV after the ADT test, illustrating that the $L1_0$-Pt(FeCoNiCuZn) MCI nanocrystals had long-term durability. DFT calculations demonstrated that the weaker Zn-O_2* bond and easily broken O—O bond of the OOH* intermediate at the active site on the $L1_0$-Pt(FeCoNiCuZn) MCI nanocrystals benefits ORR performance. The enhanced ORR performance arises not only from the ligand effect due to the regulation of the *d*-band electronic orbitals in the unique MCI structure but also from the geometric effect achieved through ultrasmall size control.

5.2. HER

Pursuing advanced electrocatalysts for HER is crucial for developing efficient and sustainable energy solutions. MCIs, with their ligand effects, geometric effect, and strain effect optimized electronic structure of Pt and downshift of the *d*-band center, permit the Pt site to attain an optimized Pt-hydrogen binding value.[60,74] This adjustment creates a delicate balance between the hydrogen adsorption and the hydrogen protonation during the HER. Furthermore, the high-entropy stabilization effect and vital multiple orbital interaction potential contribute to the stability of the HER.[47,61] For example, Saleem et al. present that the descriptor, hydrogen-adsorption free energy ΔGH*, features the thermoneutrality, $\Delta G_{H^*} \approx 0$, to represent the superior HER activity (**Figure 16a**).[61] Optimized Pt—H binding value led to rapid H* adsorption, and a highly occupied state of the *d* orbital of Pt near the Fermi level promoted electron transfer. A new *d*-electronic state in MCI leads to an improved electron environment for boosting HER activity (Figure 16b,c). In acidic media, a high-entropy stabilization effect and strong *d*–*d* interaction in the MCI structure led to superior stability (Figure 16d). Furthermore, Liu et al. introduce an MCI catalyst with a military composition designed for HER (Figure 16e).[60] The MCI catalyst, FeCoNiAlTi, forming an $L1_2$-type ordered structure, exhibits an overpotential of 88.2 mV at 10 mA cm^{-2} in alkaline conditions (Figure 16f). MCI structures with distinguished site isolation (geometric effects) can effectively avoid Al-rich surfaces. The isolated Al atoms coordinating with other elements, e.g., Fe, Co, Ni, provide a beneficial ΔG_{H^*} value (approaching zero) for the Heyrovsky step with the hydrogen adsorption and desorption. Additionally, the center of the *d* orbital partial DOS for the coordinated sites in the MCI significantly shifts farther from the Fermi level, further confirming the weakening of hydrogen adsorption. Notably, the time-dependent catalytic stability of the MCI indicates superior stability (Figure 16g), which attributes the high-entropy effects.

Overall, these studies underscore the importance of structural and compositional innovation in the quest for efficient and cost-effective electrocatalysts for HER. The ordered structures achieved in both approaches are vital for ensuring the stability and efficiency of the catalysts. Future research should aim to refine synthesis methods, broaden compositional exploration, and address scalability to bring these promising materials closer to practical application.

5.3. Alcohol and Acid Oxidation Reaction

The electrochemical oxidation of small molecules (e.g., FAOR, MOR, EOR) represents typical anode reactions in fuel cells. Direct formic acid and alcohol fuel cells are emphasized due to their advantage of eliminating hydrogen storage. These complex reactions involve slow kinetics and multiple electron transfers, along with challenging adsorption and desorption processes of reaction intermediates. In the case of EOR, the C_1 pathway implies a complete oxidation of ethanol accompanied by the transfer of 12 electrons and the generation of carbon dioxide or carbonate. On the one hand, C_1 pathway includes direct and indirect, which means different intermediate generations; on the other hand, the C_1 pathway is often inhibited by the C_2 pathway, which provides for two-electron transfers to acetaldehyde or four electron transfers to acetic acid. Precious metals, especially platinum group metals of Pt and Pd, have been shown to have excellent intrinsic activity and are highly desired candidates. The principal

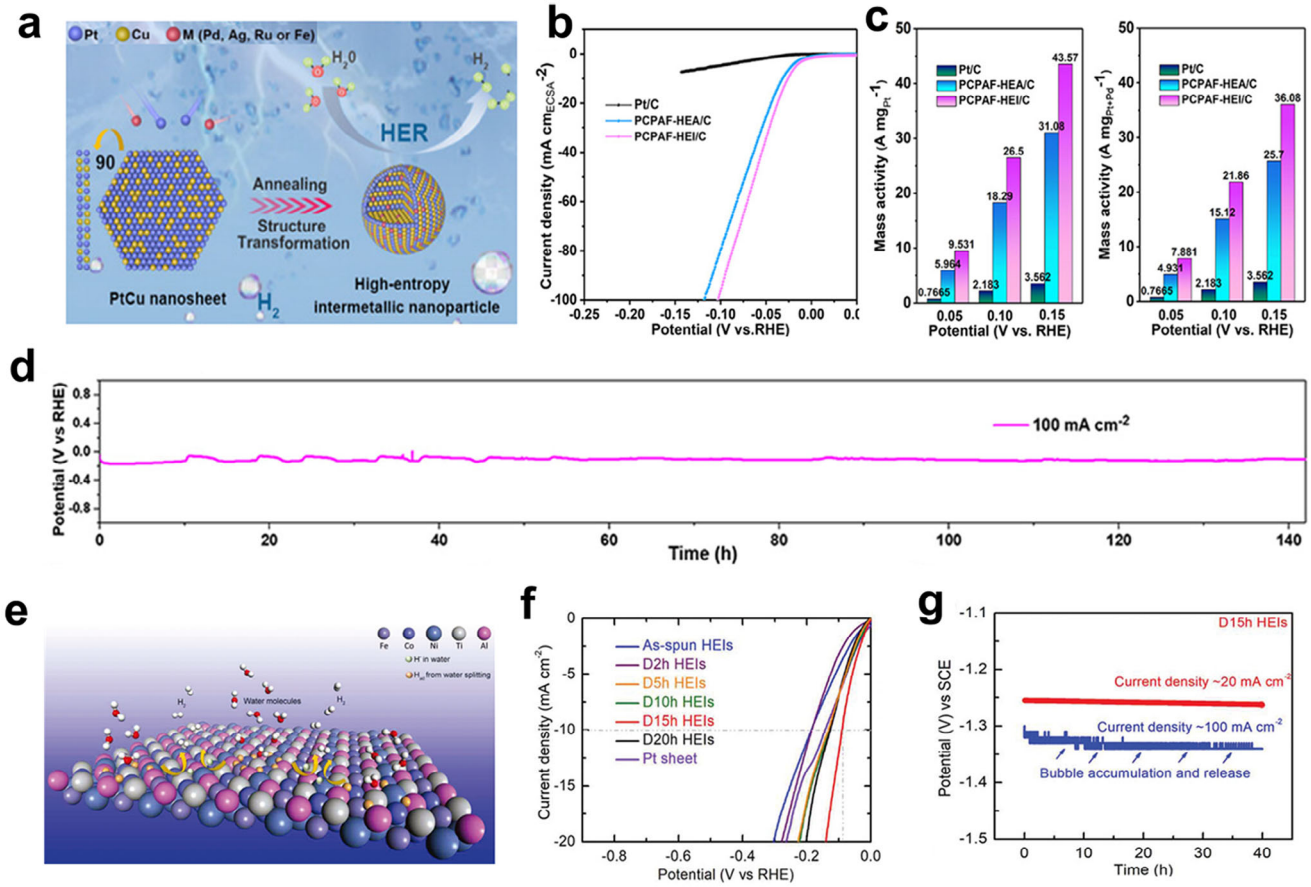

Figure 16. a) Schematic illustration of the synthesis of $L1_1$-PtCu NPs. b) Comparison of the HER polarization curves. c) Mass activities of commercial Pt/C, PtCuPdAgFe-HEA/C, and PtCuPdAgFe-MCI/C. d) Stability test of time-dependent overpotential curve of PtCuPdAgFe-MCI/C. Reproduced with permission.[61] Copyright 2024, Wiley-VCH. e) Schematic diagram of the HER process for the $L1_2$-FeCoNiAlTi MCI. f) Polarization curves. g) Time-dependent catalytic stability of the $L1_2$-FeCoNiAlTi MCI. Reproduced with permission.[60] Copyright 2020, Wiley-VCH.

contradiction is that the current industrial hydrogen production process will inevitably introduce trace amounts of carbon monoxide, and both Pt/Pd catalysts will be severely deactivated due to poisoning. Numerous findings have shown that introducing an oxyphilic element into platinum group metal catalysts can effectively modulate the electronic structure and is a highly efficient strategy to alleviate the poisoning. MCI catalysts ensure uniform dilution and complete isolation of all Pt or Pd sites (geometric effect) compared to conventional alloys. In addition to inhibiting the poisoning phenomenon, more importantly, the MCI catalyst has a more substantial strain effect, adequate optimization of the *d*-band center, ensures a more appropriate adsorption strength of crucial intermediates in the complex multi-electron transfer system, optimizes the reaction kinetics, improve the product selectivity. Therefore, developing advanced MCI catalysts provides excellent scope for electronic structure modulation and performance optimization.

Ternary intermetallic compounds-PtSnBi nanoplates were prepared using a one-pot wet chemical method by Quan et al. (**Figure 17a**).[66] The isolated Pt sites avoided the possibility of CO poisoning due to formic acid dehydration in conventional Pt-based catalysts, and the long-range ordered atomic arrangement of the nanoplates ensured that the dehydrogenation step directly oxidizes formic acid to form CO_2. Thanks to the synergistic effect of the three metals, the FAOR performance of the PtSnBi nanoplates was significantly superior to that of the binary PtBi and PtSn intermetallic compounds (Figure 17b). The mass activity of $Pt_{45}Sn_{25}Bi_{30}$ nanoplates was as high as 4394 mA mg_{Pt}^{-1} and retained 78% of the initial activity after 4000 cycles (Figure 17c–e). Reducing the size of the catalyst is crucial to improve intrinsic activity. Wang et al.[35] constructed an ultrasmall $(PtPdIrRu)_2(FeCu)$ MCI, starting with PtFe as the parent phase. They substituted some Pt atoms with Pd, Ir, or Ru, and replaced some Fe atoms with Cu. This resulted in a material with a more negative Pt valence state, a diluted distribution of precious metal sites, and an average particle size of less than 2 nm. At electrocatalytic FAOR, the intrinsic activity of ultrasmall MCIs is significantly better than that of Pt and Pt_2FeCu, and the durability is also optimized (Figure 17f–h). Theoretical calculations show that MCI shows much weaker binding of CO* on Pt sites and slow diffusion of CO* between sites compared to pure Pt (Figure 17i), which is much more strongly bound and readily diffuses over larger Pt atom groups.

At present, some progress has been made in optimizing alcohol oxidation by using polymetallic intermetallic electrocatalysts.

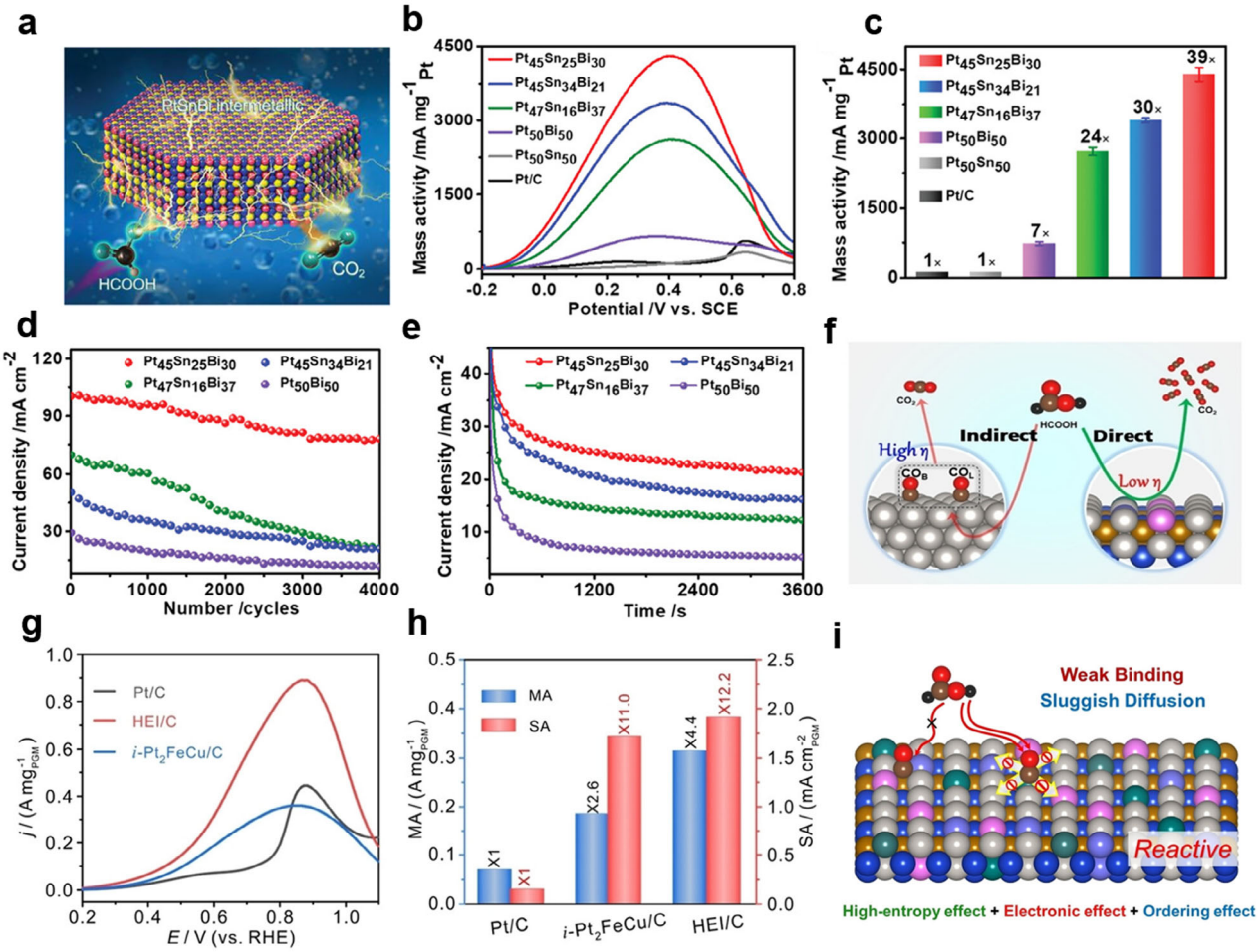

Figure 17. a) Schematic illustration of atomic Pt/Sn/Bi arrangement. b) Polarization curves of different catalysts toward FAOR. c) Pt mass-normalized activities for FAOR. d) The changes in mass activities before and after long-term potential cycles. e) The chromoamperometric curves for 3600 s. Reproduced with permission.[66] Copyright 2019, Wiley-VCH. f) Schematic diagram for the main FAOR pathway on the Pt and $(PtPdIrRu)_2FeCu$ MCI. g) Comparison of polarization curves, mass activity, and specific activity of $(PtPdIrRu)_2FeCu/C$ MCI, Pt_2FeCu/C, and Pt/C for FAOR. h) Mass activity and specific activity for FAOR at 0.6 V. i) Schematic illustration for the CO* adsorption and diffusion of MCI surfaces. Reproduced with permission.[35] Copyright 2024, Wiley-VCH.

Lu et al. proposed a wet chemical epitaxial growth strategy to synthesize metastable phase Pd_3Bi intermetallic compounds with Pd_3 Pb nanocubes with cubic crystal phase (**Figure 18**a,b).[67] The resulting catalyst showed excellent catalytic performance in electrocatalytic EOR (Figure 18c), and its mass and specific activities reached 8.5 A mg_{Pt}^{-1} and 11.6 mA cm^{-2}, respectively, which were 7.5 and 3.6 times higher than commercial Pd/C, respectively. As shown in Figure 18d, after a 30000 s test at 0.66 V (versus RHE), the mass activity of $Pd_3Pb@Pd_3Bi$ nanocubes remained at 1.19 A mg_{Pd}^{-1}, significantly higher than the Pd_3 Pb nanocubes (0.14 A mg_{Pd}^{-1}) and commercial Pd/C (0.06 A mg_{Pd}^{-1}). Furthermore, the peak current density of $Pd_3Pb@Pd_3Bi$ nanocubes decayed only by 3.5% after 30 000 s of testing (Figure 18e). These results highlight the superior stability of the $Pd_3Pb@Pd_3Bi$ nanocubes under alkaline conditions. Quan et al. synthesized hexagonal-close-packed (*hcp*) PtRhBiSnSb MCI nanoplates with inherently isolated Pt, Rh, Bi, Sn, and Sb atoms to promote the electrochemical oxidation of liquid fuels.[55] The *hcp*-type PtBi MCIs combine the structural advantages of HEAs and intermetallic compounds, increase the Pt—Pt distance and have stronger interatomic interactions, which shows excellent activity comparison with Pt/C (Figure 18f), binary PtBi and quaternary PtBiSnSb nanoplates in MOR, EOR, and glycerol oxidation reaction (Figure 18g–i). The correlation data show that introducing Rh for the high-entropy nanoplate not only improves the electron transfer but also forms the optimal *d*-band center and improves the electrochemical AOR capacity. Wang et al. synthesized structurally ordered $L1_0$-PtRhFeNiCu MCIs loaded by multi-walled carbon nanotubes, demonstrating excellent electrocatalytic activity and CO tolerance in EOR compared with a HEA composed of the same elements (Figure 18j,k).[114] Theoretical and experimental evidence shows that the MCIs have more vital C—C bond-breaking ability than the corresponding HEAs and Pt/C, while the author built direct alcohol fuel cell devices with PtRhFeNiCu as the anode, indicating the potential utilization value of PtRhFeNiCu.

In conclusion, as shown in **Table 2**, a comparison between the performance of MCI and binary intermetallic compounds reveals that MCI generally exhibits superior catalytic performance,

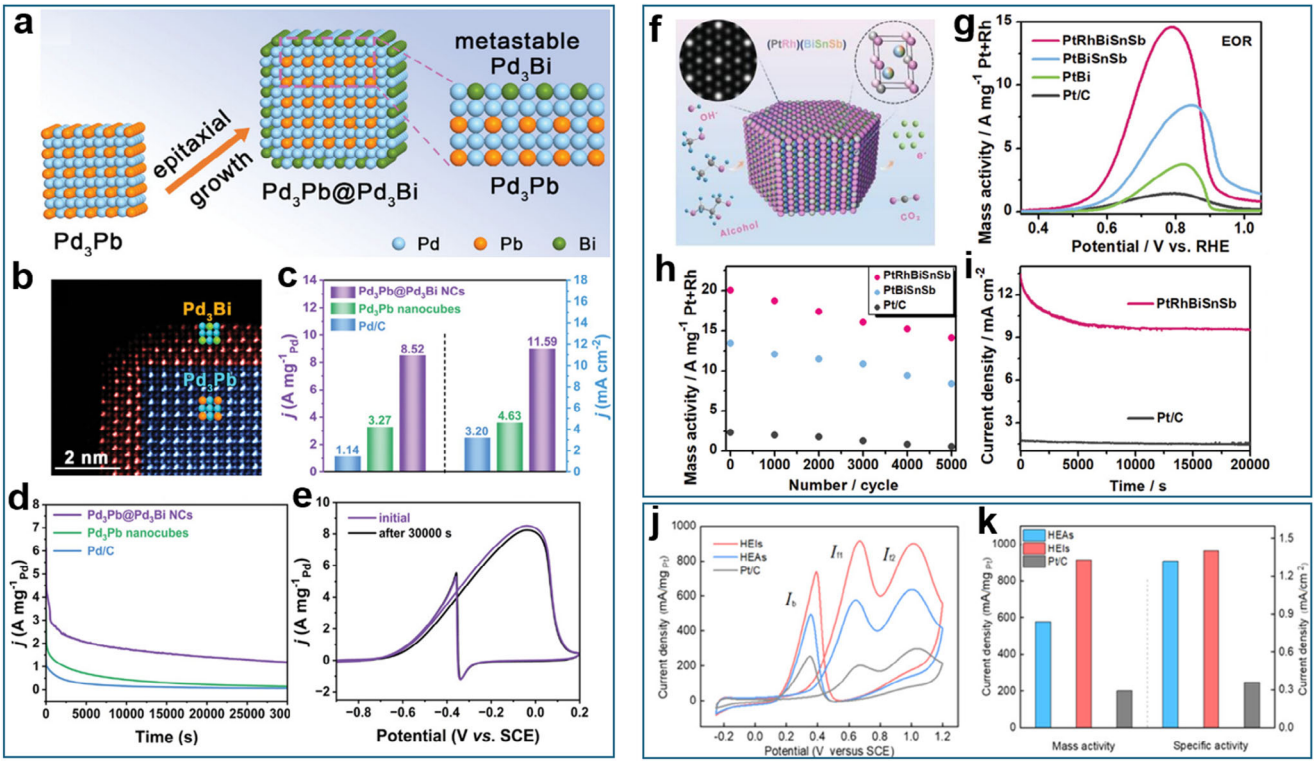

Figure 18. a) Schematic illustration of the synthesis process from Pd_3Pb nanocubes to $Pd_3Pb@Pd_3Bi$ nanocrystals. b) HAADF-STEM image: Pd_3Pb (blue) and Pd_3Bi (red). c) Histogram of mass and specific activities of different catalysts. d) The stability test of different catalysts. e) CV curves of $Pd_3Pb@Pd_3Bi$ nanocrystals before (purple) and after (black) the i-t test. Reproduced with permission.[115] Copyright 2024, Wiley-VCH. f) Schematic illustration of Pt/Rh/Bi/Sn/Sb atoms. g) EOR polarization curves of different catalysts were recorded. h) The changes in mass activities of different catalysts before and after long-term potential cycling. i) Long-term chronoamperometry for MOR of different catalysts. Reproduced with permission.[55] Copyright 2022, Wiley-VCH. j) Comparison of polarization curves. k) Specific activities and mass activities of the HEAs, MCIs, and Pt/C. Reproduced with permission.[114] Copyright 2022, Wiley-VCH.

including higher mass activity, specific activity, and half-wave potential. In some cases, these differences are as much as six times greater. This enhanced catalytic performance can be attributed to the optimization of MCIs electronic structure and the synergistic effects between its multiple elements, which collectively improve its overall efficiency compared to binary intermetallic compounds.

6. Conclusion and Perspectives

Over the past 20 years, significant progress has been made in the vast compositional and microscopic structural of MCIs. We have summarized the most recent advancements in Pt-based MCI nanocrystals. First, we analyzed the structural characteristics of MCIs, entropy and enthalpy, and their thermodynamic and kinetic transition parameters. Further, we explored the effects generated by MCIs, specifically the ligand, geometric, and strain effects. In terms of synthesis methods, we discussed the advantages and disadvantages of synthesis methods, including thermal annealing, Joule heating, wet chemistry, and other methods. The thermal annealing method has the drawback of particle sintering, but this issue can be improved by enhancing the interaction between particles and the substrate or doping with low melting point metals. The wet-chemical method effectively controls the composition ratio. Still, due to the low synthesis temperature, the degree of order is low, failing to overcome the energy barrier of the disorder-to-order transition. The cutting-edge manufacturing protocol ultrafast Joule heating method is highly efficient, but systematically synthesizing MCIs with different components remains challenging. Based on MCIs formed between the platinum group metals and elements from *d*-block, *p*-block, and *f*-block, respectively, we analyzed in detail the impact of multiple orbital hybridizations on the electronic structure and the *d*-band center shift of active sites. On this basis, we further examined their effects on catalytic performance. The conclusion is that with multiple and different orbital hybridizations, the degree of orbital overlap varies, resulting in different chemical bond strengths. Meanwhile, the shift of the *d*-band center of active sites to varying degrees modulates the catalytic activity. In all, this field continuously sparks new research questions and major scientific themes. There are still challenges and opportunities in various areas, as illustrated in **Figure 19**, which presents the proposed framework for the conclusions and future perspectives of MCIs.

1. Expanding the composition space and configuration design of MCIs

Current research mainly focuses on Pt-3*d* transition metal MCIs, limited Pt-*p* block metal or Pt-*f* block metal MCI with

Table 2. Comparison of properties between MCIs and binary intermetallic compounds.

Component	Catalysts	Performance	Performance comparison	Refs.
MCI	$Pt(FeCoNiCu)_3$ for ORR	MA [a] = 2.71 ± 0.11 A mg^{-1}_{Pt} SA [b] = 3.82 ± 0.44 mA cm^{-2}	MA:2.6 times SA:1.8 times	[44]
Binary	$PtCu_3$ for ORR	MA = 1.02 ± 0.13 A mg^{-1}_{Pt} SA = 2.12 ± 0.33 mA cm^{-2}	–	
MCI	$Pt_4FeCoNiCu$ for ORR	$E_{1/2}$ [c] = 0.930 V MA = 1.0 A mg^{-1}_{Pt} SA = 2.8 mA cm^{-2}	$E_{1/2}$: 0.01V MA:1.8 times SA:2.0 times	[46]
Binary	PtCo for ORR	$E_{1/2}$ = 0.920 V MA≈ 0.55 A mg^{-1}_{Pt} SA≈1.45 mA cm^{-2}	–	
MCI	$Pt(FeCoNiCuZn)_3$ for ORR	$E_{1/2}$ = 0.922 V MA = 0.70 A mg^{-1}_{Pt} SA = 1.34 mA cm^{-2}	$E_{1/2}$: 0.02V MA:2.1 times SA:1.3 times	[108]
Binary	$PtCu_3$ for ORR	$E_{1/2}$ = 0.902 V MA = 0.33 A mg^{-1}_{Pt} SA = 1.01 mA cm^{-2}	–	
MCI	Ga-Pt_5Ce for ORR	MA = 0.45 A mg^{-1}_{Pt} SA = 0.55 mA cm^{-2}	MA:1.8 times SA:1.0 times	[51]
Binary	Pt_5Ce for ORR	MA = 0.24 A mg^{-1}_{Pt} SA = 0.52 mA cm^{-2}	–	
MCI	Pt_2CoCu for ORR	MA ≈ 3.0 A mg^{-1}_{Pt}	MA:1.5 times	[110]
Binary	PtCo for ORR	MA<2.0 A mg^{-1}_{Pt}	–	
MCI	$Ga_{0.1}$- PtCo for ORR	MA = 0.345±0.010 A mg^{-1}_{Pt}	MA:2.3 times	[50]
Binary	PtCo for ORR	MA = 0.147±0.014 A mg^{-1}_{Pt}	–	
MCI	$Pt_{1.8}Pd_{0.2}CuGa$ for MOR	MA = 11.13 A mg^{-1}_{PGM}	MA:2.1 times	[54]
Binary	PtCu for MOR	MA = 5.23 A mg^{-1}_{PGM}	–	
MCI	PtRhBiSnSb for MOR	MA = 19.529 A mg^{-1}_{Pt+Rh}	MA:3.9 times	[55]
Binary	PtBi for MOR	MA~4.9 A mg^{-1}_{Pt+Rh}	–	
MCI	$Pt_3Sn_{0.5}Mn_{0.5}$ for MOR	MA = 2.39 A mg^{-1}_{Pt} SA = 4.78 mA cm^{-2}	MA:1.8 times SA:2.0 times	[70]
Binary	Pt_3Mn for MOR	MA = 1.32 A mg^{-1}_{Pt} SA = 2.35 mA cm^{-2}	–	
MCI	$Pt_{45}Sn_{25}Bi_{30}$ for FAOR	MA = 4.394 A mg^{-1}_{Pt}	MA:6.0 times	[66]
Binary	PtBi for FAOR	MA≈0.732 A mg^{-1}_{Pt}	–	

[a] Mass activities; [b] Specific activities; [c] $E_{1/2}$ = Half-wave potential.

$L1_0$ and $L1_2$ configurations. Although these studies have demonstrated the great potential of MCI nanocrystals in the field of electrocatalysis, the narrow composition space limits further exploration and optimization. To break through this bottleneck, it is essential to expand the composition space and configuration design of MCI to develop new nanomaterials with excellent catalysis performance. First, including a wider variety of elements, such as more *p*-block metals and *f*-block rare earth metals, should be considered to screen and optimize these elemental combinations systematically. Its potential reveals materials with enhanced catalytic activity, improved stability, and better selectivity. For example, rationally combining *d*-block transition metals with *p*-block low-melting-point metals and *f*-block rare earth metals could yield unexpected performance enhancements. Second, exploring a broader range of structures beyond the $L1_0$ and $L1_2$ configurations is crucial. Other ordered structures, such as B2, $L2_1$, etc., are also worthy of in-depth investigations. These structural types may exhibit unique physical and chemical properties under different element combinations, thereby further improving the catalytic performance of MCI.

2. Emerging MCI design principles and guidelines

The primary issue mentioned above to expand the MCI is the lack of general design principles and guidelines for MCI design, specifically, how to predict and control the phase structure of MCI nanocrystals. The complexity of multiple elemental compositions complicates predictions. Although there are phase formation rules for HEA, they are mainly related to parameters such as mixing entropy, mixing enthalpy, atomic radius, valence electron concentration, and electronegativity. These rules do not directly apply to MCIs due to their characteristics of ordered superlattice structures and sublattice high-entropy effects. For example, forming a HEA nanocrystal requires a negative mixing enthalpy, different electronegativity, and high mixing entropy. However, the

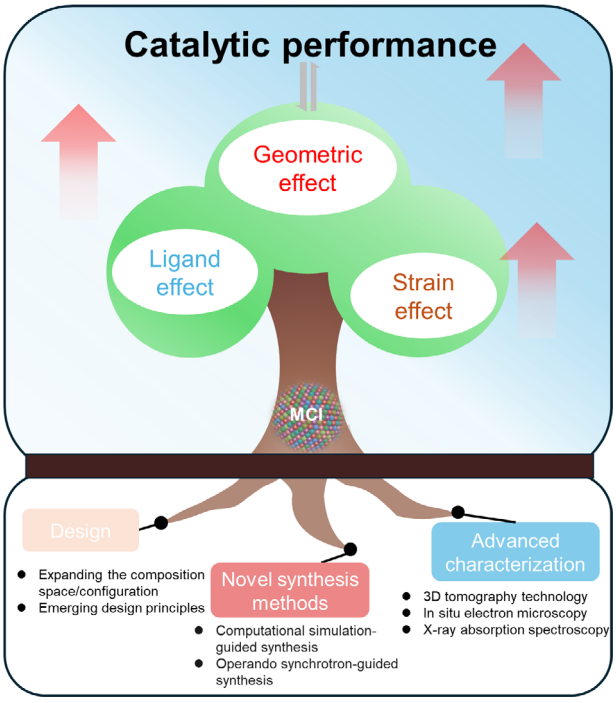

Figure 19. Proposed framework for the conclusions and further perspectives of the MCIs.

empirical parameters of existing HEA formation rules do not apply to MCIs.

Traditionally used alloy design methods include the parameterization method, first principal calculation, and CALPHAD method. Although the CALPHAD method is considered an effective alloy design method, reliable thermodynamic databases are essential for accurate calculation. However, there is still a lack of an effective thermodynamic database for MCI. Although some parameterization methods can predict the thermodynamics and kinetics of the ordering process, these methods are only valid for some specific alloy systems and lack systematicity. It is also necessary to explore the phase formation criteria of MCI. Fortunately, advanced technologies such as high-throughput computing and machine learning can accelerate the exploration of component spaces and configuration design for MCI. High-throughput computing can screen out potential high-performance nanomaterials combined with experimental verification, significantly improving research efficiency. Machine learning algorithms can extract valuable patterns and insights from large volumes of computational and experimental data, guiding the design and optimization of new materials.

3. Developing novel synthesis methods for MCIs

The synthesis of MCI primarily relies on trial-and-error, which is inefficient, time-consuming, and costly, significantly limiting the rapid development and application of MCIs. Traditional trial-and-error methods often require repeated adjustment of reaction conditions and exploration of different synthesis pathways, consuming substantial time and resources while making it challenging to ensure the desired material performance. Therefore, it is urgent to develop more efficient synthesis methods. As a cutting-edge manufacturing protocol, Joule heating technology can rapidly synthesize materials quickly through rapid heating and cooling while accurately controlling the crystallization process of materials to avoid particle growth and structural disorder. This method can significantly enhance synthesis efficiency, shorten the development cycle, and reduce preparation costs. Moreover, integrating synthesis strategies with computational simulation-guided inverse design and real-time control using Operando Synchrotron techniques further demonstrates promising potential. By coupling synthesis reactors with synchrotron X-ray facilities, such as X-ray absorption spectroscopy and diffraction, it becomes feasible to monitor atomic ordering dynamics in real time. Machine learning algorithms enable continuous adjustment of synthesis parameters through feedback loops, achieving high precision and resolving sub-second phase evolution for on-demand MCI crystallization.

4. Building precise analyses methodology of complex structures of MCIs

Due to their multi-component and complex structures, characterization methods such as X-ray diffraction and aberration-corrected HR-TEM are no longer sufficient for accurately analyzing MCIs. Advanced characterization technologies are essential to explore. For example, 3D tomography technology can provide new perspectives for the structural analysis of MCIs. Through 3D tomography, the position of atoms can be accurately located in 3D space, and the 3D atomic structure image of the material can be reconstructed. This is of great significance for revealing the complex structural characteristics of MCIs, such as atomic arrangement, defect distribution, and interface structure. 3D tomography can provide more detailed information to understand the local chemical environment and lattice distortion of materials. In addition, combined with other characterization techniques, such as in situ electron microscopy and X-ray absorption spectroscopy, multi-scale and multi-dimensional analysis of material structure and performance can be achieved, providing strong support for in-depth research on the structure-performance relationship of MCIs.

5. Establishing the relationship between structure and catalytic performance of MCIs

The unique structural characteristics of MCIs endow them with excellent potential for application in electrocatalysis. To fully explore their catalytic performance, systematically studying the structure-performance relationship of MCIs is crucial. By intensely studying the crystal structure characteristics and performance of different MCIs in various catalytic reactions, it can be revealed how their structural features influence catalytic performance. Specifically, the mechanism of action of high-entropy, ligand, geometric, and strain effects in the catalytic process can be studied through advanced characterization techniques discussed above and DFT calculation. We can accelerate the design and development of novel and efficient electrocatalysts by systematically constructing a structure-performance database for MCIs and employing advanced data analysis methods such as machine learning. This approach can potentially provide

breakthrough catalytic materials for energy, environmental, and other applications.

Acknowledgements

Y.D. acknowledged the financial support from the National Key R&D Program of China (2022YFB2502104). M.C. acknowledged the Project of the National Laboratory of Solid State Microstructures (M37011); and the National Natural Science Foundation of China (52403308).

Conflict of Interest

The authors declare no conflict of interest.

Keywords

electrocatalysis, multi-component intermetallic, nanocrystals, orbital hybridization, synthesis strategies

Received: January 12, 2025
Revised: March 16, 2025
Published online:

[1] J. W. Yeh, S. K. Chen, S. J. Lin, J. Y. Gan, T. S. Chin, T. T. Shun, C. H. Tsau, S. Y. Chang, *Adv. Eng. Mater.* **2004**, *6*, 299.
[2] B. Cantor, I. T. H. Chang, P. Knight, A. J. B. Vincent, *Mater. Sci. Eng., A* **2004**, *375–377*, 213.
[3] C.-J. Tong, Y.-L. Chen, J.-W. Yeh, S.-J. Lin, S.-K. Chen, T.-T. Shun, C.-H. Tsau, S.-Y. Chang, *Metall. Mater. Trans. A* **2005**, *36*, 881.
[4] D. B. Miracle, O. N. Senkov, *Acta Mater.* **2017**, *122*, 448.
[5] E. P. George, D. Raabe, R. O. Ritchie, *Nat. Rev. Mater.* **2019**, *4*, 515.
[6] S. Wei, S. J. Kim, J. Kang, Y. Zhang, Y. Zhang, T. Furuhara, E. S. Park, C. C. Tasan, *Nat. Mater.* **2020**, *19*, 1175.
[7] L. Du, H. Xiong, H. Lu, L.-M. Yang, R.-Z. Liao, B. Y. Xia, B. You, *Exploration* **2022**, *2*, 20220024.
[8] A. Asghari Alamdari, H. Jahangiri, M. B. Yagci, K. Igarashi, H. Matsumoto, A. Motallebzadeh, U. Unal, *ACS Appl. Energy Mater.* **2024**, *7*, 2423.
[9] Z. W. Chen, J. Li, P. Ou, J. E. Huang, Z. Wen, L. Chen, X. Yao, G. Cai, C. C. Yang, C. V. Singh, Q. Jiang, *Nat. Commun.* **2024**, *15*, 359.
[10] L. He, M. Li, L. Qiu, S. Geng, Y. Liu, F. Tian, M. Luo, H. Liu, Y. Yu, W. Yang, S. Guo, *Nat. Commun.* **2024**, *15*, 2290.
[11] S. Liu, Y. Wang, T. Jiang, S. Jin, M. Sajid, Z. Zhang, J. Xu, Y. Fan, X. Wang, J. Chen, Z. Liu, X. Zheng, K. Zhang, Q. Nian, Z. Zhu, Q. Peng, T. Ahmad, K. Li, W. Chen, *ACS Nano* **2024**, *18*, 4229.
[12] S. K. Verma, S. S. Mishra, N. K. Mukhopadhyay, T. P. Yadav, *Int. J. Hydrogen Energy* **2024**, *50*, 749.
[13] H. Lv, X. Guo, L. Sun, D. Xu, B. Liu, *Sci. China Chem.* **2021**, *64*, 245.
[14] Y. Yao, Z. Huang, P. Xie, S. D. Lacey, R. J. Jacob, H. Xie, F. Chen, A. Nie, T. Pu, M. Rehwoldt, D. Yu, M. R. Zachariah, C. Wang, R. Shahbazian-Yassar, J. Li, L. Hu, *Science* **2018**, *359*, 1489.
[15] A. Sarkar, Q. Wang, A. Schiele, M. R. Chellali, S. S. Bhattacharya, D. Wang, T. Brezesinski, H. Hahn, L. Velasco, B. Breitung, *Adv. Mater.* **2019**, *31*, 1806236.
[16] S. S. Aamlid, M. Oudah, J. r. Rottler, A. M. Hallas, *J. Am. Chem. Soc.* **2023**, *145*, 5991.
[17] A. Sarkar, L. Velasco, D. Wang, Q. Wang, G. Talasila, L. de Biasi, C. Kübel, T. Brezesinski, S. S. Bhattacharya, H. Hahn, *Nat. Commun.* **2018**, *9*, 3400.
[18] M. Cui, C. Yang, B. Li, Q. Dong, M. Wu, S. Hwang, H. Xie, X. Wang, G. Wang, L. Hu, *Adv. Energy Mater.* **2021**, *11*, 2002887.
[19] L. Lin, K. Wang, A. Sarkar, C. Njel, G. Karkera, Q. Wang, R. Azmi, M. Fichtner, H. Hahn, S. Schweidler, *Adv. Energy Mater.* **2022**, *12*, 2103090.
[20] C. R. McCormick, R. E. Schaak, *J. Am. Chem. Soc.* **2021**, *143*, 1017.
[21] S. K. Nemani, B. Zhang, B. C. Wyatt, Z. D. Hood, S. Manna, R. Khaledialidusti, W. Hong, M. G. Sternberg, S. K. R. S. Sankaranarayanan, B. Anasori, *ACS Nano* **2021**, *15*, 12815.
[22] L. Feng, W. G. Fahrenholtz, D. W. Brenner, *Annu. Rev. Mater. Res.* **2021**, *51*, 165.
[23] Z. Du, C. Wu, Y. Chen, Z. Cao, R. Hu, Y. Zhang, J. Gu, Y. Cui, H. Chen, Y. Shi, J. Shang, B. Li, S. Yang, *Adv. Mater.* **2021**, *33*, 2101473.
[24] Y. Yao, Q. Dong, A. Brozena, J. Luo, J. Miao, M. Chi, C. Wang, I. G. Kevrekidis, Z. J. Ren, J. Greeley, G. Wang, A. Anapolsky, L. Hu, *Science* **2022**, *376*, abn3103.
[25] G. Cao, J. Liang, Z. Guo, K. Yang, G. Wang, H. Wang, X. Wan, Z. Li, Y. Bai, Y. Zhang, J. Liu, Y. Feng, Z. Zheng, C. Lu, G. He, Z. Xiong, Z. Liu, S. Chen, Y. Guo, M. Zeng, J. Lin, L. Fu, *Nature* **2023**, *619*, 73.
[26] S. Gao, S. Hao, Z. Huang, Y. Yuan, S. Han, L. Lei, X. Zhang, R. Shahbazian-Yassar, J. Lu, *Nat. Commun.* **2020**, *11*, 2016.
[27] G. Feng, Y. Pan, D. Su, D. Xia, *Adv. Mater.* **2024**, *36*, 2309715.
[28] Y. Sun, S. Dai, *Sci. Adv.* **2021**, *7*, abg1600.
[29] J. Liang, G. Cao, M. Zeng, L. Fu, *Chem. Soc. Rev.* **2024**, *53*, 6021.
[30] H. Wu, S. Huang, F. Li, Y. Ma, X. Meng, *Chem. Eng. J.* **2024**, *499*, 156419.
[31] J. Liu, C. Lee, Y. Hu, Z. Liang, R. Ji, X. Y. D. Soo, Q. Zhu, Q. Yan, *SmartMat* **2023**, *4*, 1210.
[32] M. Cui, C. Yang, S. Hwang, M. Yang, S. Overa, Q. Dong, Y. Yao, A. H. Brozena, D. A. Cullen, M. Chi, T. F. Blum, D. Morris, Z. Finfrock, X. Wang, P. Zhang, V. G. Goncharov, X. Guo, J. Luo, Y. Mo, F. Jiao, L. Hu, *Sci. Adv.* **2022**, *8*, abm4322.
[33] C.-L. Yang, L.-N. Wang, P. Yin, J. Liu, M.-X. Chen, Q.-Q. Yan, Z.-S. Wang, S.-L. Xu, S.-Q. Chu, C. Cui, H. Ju, J. Zhu, Y. Lin, J. Shui, H.-W. Liang, *Science* **2021**, *374*, 459.
[34] X. Liu, X. Wang, C. Mao, J. Qiu, R. Wang, Y. Liu, Y. Chen, D. Wang, *Angew. Chem., Int. Ed.* **2024**, *8*, 202408109.
[35] T. Shen, D. Xiao, Z. Deng, S. Wang, L. An, M. Song, Q. Zhang, T. Zhao, M. Gong, D. Wang, *Angew. Chem., Int. Ed.* **2024**, *63*, 202403260.
[36] T. Chen, C. Qiu, X. Zhang, H. Wang, J. Song, K. Zhang, T. Yang, Y. Zuo, Y. Yang, C. Gao, W. Xiao, Z. Jiang, Y. Wang, Y. Xiang, D. Xia, *J. Am. Chem. Soc.* **2024**, *146*, 1174.
[37] H. Lv, B. Liu, *Chem. Soc. Rev.* **2024**, *53*, 11321.
[38] Z. Liu, L. Zhang, *J. Alloys Compd.* **2024**, *981*, 173716.
[39] J. Li, S. Sun, *Acc. Chem. Res.* **2019**, *52*, 2015.
[40] L. M. C. Pinto, M. F. Juárez, A. C. D. Ângelo, W. Schmickler, *Electrochim. Acta* **2014**, *116*, 39.
[41] F. Lin, M. Li, L. Zeng, M. Luo, S. Guo, *Chem. Rev.* **2023**, *123*, 12507.
[42] K. Wang, J. Huang, H. Chen, Y. Wang, W. Yan, X. Yuan, S. Song, J. Zhang, X. Sun, *Electrochem. Energy Rev.* **2022**, *5*, 17.
[43] C. M. Clausen, J. K. Pedersen, T. A. A. Batchelor, J. Rossmeisl, *Nano Res.* **2022**, *15*, 4775.
[44] S.-B. Li, P. Yin, C. Xu, K.-Z. Xue, Y. Kong, M. Zuo, W.-Q. Zhang, H.-W. Liang, *Small* **2024**, *20*, 2401134.
[45] Y. Wang, N. Gong, H. Liu, W. Ma, K. Hippalgaonkar, Z. Liu, Y. Huang, *Adv. Mater.* **2023**, *35*, 2302067.
[46] X. Zeng, Y. Jing, S. Gao, W. Zhang, Y. Zhang, H. Liu, C. Liang, C. Ji, Y. Rao, J. Wu, B. Wang, Y. Yao, S. Yang, *Nat. Commun.* **2023**, *14*, 7414.
[47] S. Shen, H. Zhang, K. Song, Z. Wang, T. Shang, A. Gao, Q. Zhang, L. Gu, W. Zhong, *Angew. Chem., Int. Ed.* **2024**, *63*, 202315340.
[48] F. Xing, J. Ma, K.-i. Shimizu, S. Furukawa, *Nat. Commun.* **2022**, *13*, 5065.
[49] Y. Nakaya, E. Hayashida, H. Asakura, S. Takakusagi, S. Yasumura, K.-i. Shimizu, S. Furukawa, *J. Am. Chem. Soc.* **2022**, *144*, 15944.

[50] R.-Y. Shao, X.-C. Xu, Z.-H. Zhou, W.-J. Zeng, T.-W. Song, P. Yin, A. Li, C.-S. Ma, L. Tong, Y. Kong, H.-W. Liang, *Nat. Commun.* **2023**, *14*, 5896.
[51] Z.-J. Zou, S.-Y. Yin, Y. Tang, S.-L. Zhong, L. Wang, S.-L. Xu, H.-W. Liang, *Nano Res.* **2024**, *17*, 8112.
[52] J. Liang, Y. Wan, H. Lv, X. Liu, F. Lv, S. Li, J. Xu, Z. Deng, J. Liu, S. Zhang, Y. Sun, M. Luo, G. Lu, J. Han, G. Wang, Y. Huang, S. Guo, Q. Li, *Nat. Mater.* **2024**, *23*, 1259.
[53] X. Liu, Z. Zhao, J. Liang, S. Li, G. Lu, C. Priest, T. Wang, J. Han, G. Wu, X. Wang, Y. Huang, Q. Li, *Angew. Chem., Int. Ed.* **2023**, *62*, 202302134.
[54] K. Xu, L. Liang, T. Li, M. Bao, Z. Yu, J. Wang, S. M. Thalluri, F. Lin, Q. Liu, Z. Cui, S. Song, L. Liu, *Adv. Mater.* **2024**, *36*, 2403792.
[55] W. Chen, S. Luo, M. Sun, X. Wu, Y. Zhou, Y. Liao, M. Tang, X. Fan, B. Huang, Z. Quan, *Adv. Mater.* **2022**, *34*, 2206276.
[56] J. Qin, P. Zou, R. Zhang, C. Wang, L. Yao, H. L. Xin, *ACS Sustainable Chem. Eng.* **2022**, *10*, 14024.
[57] G. Zhu, Y. Jiang, H. Yang, H. Wang, Y. Fang, L. Wang, M. Xie, P. Qiu, W. Luo, *Adv. Mater.* **2022**, *34*, 2110128.
[58] W. Zhao, B. Chi, L. Liang, P. Yang, W. Zhang, X. Ge, L. Wang, Z. Cui, S. Liao, *ACS Catal.* **2022**, *12*, 7571.
[59] Y. Wang, X.-Y. Zhang, H. He, J.-J. Chen, B. Liu, *Adv. Energy Mater.* **2024**, *14*, 2303923.
[60] Z. Jia, T. Yang, L. Sun, Y. Zhao, W. Li, J. Luan, F. Lyu, L.-C. Zhang, J. J. Kruzic, J.-J. Kai, J. C. Huang, J. Lu, C. T. Liu, *Adv. Mater.* **2020**, *32*, 2000385.
[61] S. Zheng, J. Hu, R. Feng, J. Xu, Y. Yu, L. Li, W. Liu, W. Zhang, F. Huo, F. Saleem, *Small Struct.* **2024**, *5*, 2300537.
[62] T. Shen, S. Chen, S. Wang, X. Huang, M. Song, X. Zhao, J. Hu, D. Wang, *Appl. Catal., B-Environ.* **2023**, *333*, 122766.
[63] L. Chen, J. Zhu, C. Xuan, W. Xiao, K. Xia, W. Xia, C. Lai, H. L. Xin, D. Wang, *J. Mater. Chem. A* **2018**, *6*, 5848.
[64] J. Zhu, Y. Yang, L. Chen, W. Xiao, H. Liu, H. D. Abruña, D. Wang, *Chem. Mater.* **2018**, *30*, 5987.
[65] T. Zhao, G. Wang, M. Gong, D. Xiao, Y. Chen, T. Shen, Y. Lu, J. Zhang, H. Xin, Q. Li, D. Wang, *ACS Catal.* **2020**, *10*, 15207.
[66] S. Luo, W. Chen, Y. Cheng, X. Song, Q. Wu, L. Li, X. Wu, T. Wu, M. Li, Q. Yang, K. Deng, Z. Quan, *Adv. Mater.* **2019**, *31*, 1903683.
[67] F. Feng, C. Ma, S. Han, X. Ma, C. He, H. Zhang, W. Cao, X. Meng, J. Xia, L. Zhu, Y. Tian, Q. Wang, Q. Yun, Q. Lu, *Angew. Chem., Int. Ed.* **2024**, *63*, 202405173.
[68] Y. Nie, Z. Li, Y. Wang, X. Zheng, L. Luo, X. Xia, S. Yang, C. Du, Y. Huang, Y. Wang, *Appl. Catal., B* **2024**, *343*, 123494.
[69] L. Liang, K. Xu, J. Liang, S. Ye, B. Zeng, Q. Liu, H. Song, L. Du, Z. Cui, *Small* **2024**, *20*, 2403557.
[70] Y. Lu, L. Liang, S. Ye, Z. Chen, W. Zhao, Z. Cui, *ACS Appl. Mater. Interfaces* **2024**, *16*, 35134.
[71] X. Ge, Y. Jing, N. Fei, K. Yan, Y. Liang, Y. Cao, J. Zhang, G. Qian, L. Li, H. Jiang, X. Zhou, W. Yuan, X. Duan, *Angew. Chem., Int. Ed.* **2024**, *136*, 202410979.
[72] J. Ma, F. Xing, Y. Nakaya, K.-i. Shimizu, S. Furukawa, *Angew. Chem., Int. Ed.* **2022**, *61*, 202200889.
[73] J. Guan, J. Zhang, X. Wang, Z. Zhang, F. Wang, *Adv. Mater.* **2023**, *35*, 2207995.
[74] C. Wu, Z. Li, S. Dong, K. Zhou, D. Ding, R. Liu, W. Pei, *ACS Appl. Nano Mater.* **2024**, *7*, 8093.
[75] T. Liu, F. Sun, M. Huang, L. Guan, *ACS Appl. Energy Mater.* **2022**, *5*, 12219.
[76] C. Li, W. Zhao, X. Lu, Z. Chen, B. Han, X. Zhang, J. Chen, Y. Shao, J. Huo, Y. Zhu, Y. Deng, S. Sun, S. Liao, *J. Energy Chem.* **2023**, *78*, 340.
[77] J. Zhang, L. Zhang, Z. Cui, *Chem. Commun.* **2021**, *57*, 11.
[78] X. Liu, Y. Wang, J. Liang, S. Li, S. Zhang, D. Su, Z. Cai, Y. Huang, L. Elbaz, Q. Li, *J. Am. Chem. Soc.* **2024**, *146*, 2033.
[79] Y. Yang, W. Xiao, X. Feng, Y. Xiong, M. Gong, T. Shen, Y. Lu, H. D. Abruña, D. Wang, *ACS Nano* **2019**, *13*, 5968.
[80] S.-G. Qin, J. Liu, Z.-Y. Chen, X.-h. Liu, H. Feng, Y. Feng, Z.-Q. Tian, P. Tsiakaras, P.-K. Shen, *Appl. Catal., B-Environ.* **2024**, *349*, 123832.
[81] J. Zheng, J. Zhang, L. Zhang, W. Zhang, X. Wang, Z. Cui, H. Song, Z. Liang, L. Du, *ACS Appl. Mater. Interfaces* **2022**, *14*, 19524.
[82] S. S. Soliman, G. R. Dey, C. R. McCormick, R. E. Schaak, *ACS Nano* **2023**, *17*, 16147.
[83] M. Nakamura, D. Wu, M. Mukoyoshi, K. Kusada, T. Toriyama, T. Yamamoto, S. Matsumura, Y. Murakami, S. Kawaguchi, Y. Kubota, H. Kitagawa, *Chem. Commun.* **2023**, *59*, 9485.
[84] J.-W. Yeh, *Overview of High-Entropy Alloys*, Springer International Publishing, Cham **2016**.
[85] D. B. Miracle, J. D. Miller, O. N. Senkov, C. Woodward, M. D. Uchic, J. Tiley, *Entropy* **2014**, *16*, 494.
[86] H. Li, Y. Han, H. Zhao, W. Qi, D. Zhang, Y. Yu, W. Cai, S. Li, J. Lai, B. Huang, *Nat. Commun.* **2020**, *11*, 5437.
[87] J. Feng, D. Chen, P. V. Pikhitsa, Y.-h. Jung, J. Yang, M. Choi, *Matter* **2020**, *3*, 1646.
[88] Y. Yao, Z. Huang, L. A. Hughes, J. Gao, T. Li, D. Morris, S. E. Zeltmann, B. H. Savitzky, C. Ophus, Y. Z. Finfrock, *Matter* **2021**, *4*, 2340.
[89] M. W. Glasscott, A. D. Pendergast, S. Goines, A. R. Bishop, A. T. Hoang, C. Renault, J. E. Dick, *Nat. Commun.* **2019**, *10*, 2650.
[90] S. Arrhenius, *Z. Phys. Chem.* **1889**, *4U*, 96.
[91] Y. Yan, J. S. Du, K. D. Gilroy, D. Yang, Y. Xia, H. Zhang, *Adv. Mater.* **2017**, *29*, 1605997.
[92] J. Liang, F. Ma, S. Hwang, X. Wang, J. Sokolowski, Q. Li, G. Wu, D. Su, *Joule* **2019**, *3*, 956.
[93] Y. Dai, P. Lu, Z. Cao, C. T. Campbell, Y. Xia, *Chem. Soc. Rev.* **2018**, *47*, 4314.
[94] D. A. Porter, K. E. Easterling, *Phase Transformations in Metals and Alloys*, Taylor & Francis Group, Boca Raton **2021**.
[95] T. L. Hill, *J. Chem. Phys.* **1962**, *36*, 3182.
[96] J. W. Mullin, *1 – The crystalline state*, Butterworth-Heinemann, Oxford **2001**.
[97] M. Cui, H. Lu, H. Jiang, Z. Cao, X. Meng, *Sci. Rep.* **2017**, *7*, 41990.
[98] M. Cui, C. Yang, S. Hwang, B. Li, Q. Dong, M. Wu, H. Xie, X. Wang, G. Wang, L. Hu, *Nano Lett.* **2022**, *22*, 255.
[99] X. Zhang, G. Lu, *J. Phys. Chem. Lett.* **2014**, *5*, 292.
[100] N. Sun, Z. Zheng, Z. Lai, J. Wang, P. Du, T. Ying, H. Wang, J. Xu, R. Yu, Z. Hu, C.-W. Pao, W.-H. Huang, K. Bi, M. Lei, K. Huang, *Adv. Mater.* **2024**, *36*, 2404772.
[101] H. Wang, Q.-F. He, Y. Yang, *Rare Met.* **2022**, *41*, 1989.
[102] T. Bligaard, J. K. Nørskov, *Electrochim. Acta* **2007**, *52*, 5512.
[103] A. Ostovari Moghaddam, R. Fereidonnejad, A. Cabot, *J. Alloys Compd.* **2023**, *960*, 170802.
[104] H. Liu, Y. Zhang, L. Zhang, X. Mu, L. Zhang, S. Zhu, K. Wang, B. Yu, Y. Jiang, J. Zhou, F. Yang, *J. Am. Chem. Soc.* **2024**, *146*, 20193.
[105] S. Furukawa, T. Komatsu, *ACS Catal.* **2017**, *7*, 735.
[106] X. Du, J. Huang, J. Zhang, Y. Yan, C. Wu, Y. Hu, C. Yan, T. Lei, W. Chen, C. Fan, J. Xiong, *Angew. Chem., Int. Ed.* **2019**, *58*, 4484.
[107] Y. Wang, Y. Yao, C. Xu, D. Tang, Y. Li, Z.-A. Qiao, H.-W. Liang, B. Liu, *Adv. Mater.* **2025**, *37*, 2416111.
[108] Q. Zhang, T. Shen, M. Song, S. Wang, J. Zhang, X. Huang, S. Lu, D. Wang, *J. Energy Chem.* **2023**, *86*, 158.
[109] W. Yan, X. Wang, M. Liu, K. Ma, L. Wang, Q. Liu, C. Wang, X. Jiang, H. Li, Y. Tang, G. Fu, *Adv. Funct. Mater.* **2024**, *34*, 2310487.

[110] P. Yin, X. Niu, S.-B. Li, K. Chen, X. Zhang, M. Zuo, L. Zhang, H.-W. Liang, *Nat. Commun.* **2024**, *15*, 415.
[111] G. Feng, F. Ning, Y. Pan, T. Chen, J. song, Y. Wang, R. Zou, D. Su, D. Xia, *J. Am. Chem. Soc.* **2023**, *145*, 11140.
[112] Y. Wang, N. Gong, G. Niu, J. Ge, X. Tan, M. Zhang, H. Liu, H. Wu, T. L. Meng, H. Xie, K. Hippalgaonkar, Z. Liu, Y. Huang, *J. Alloys Compd.* **2023**, *960*, 171039.
[113] B. Jia, B. Zhang, Z. Cai, X. Yang, L. Li, L. Guo, *eScience* **2023**, *3*, 100112.
[114] D. Wang, Z. Chen, Y. Wu, Y.-C. Huang, L. Tao, J. Chen, C.-L. Dong, C. V. Singh, S. Wang, *SmartMat* **2023**, *4*, 1117.
[115] S. Han, H. Sun, C. Ma, Q. Yun, C. He, X. Ma, H. Zhang, F. Feng, X. Meng, J. Xia, A.-L. Wang, W. Cao, Q. Lu, *Adv. Funct. Mater.* **2024**, *34*, 2403023.

Mingjin Cui is a distinguished recipient of the Young Elite Scientists Sponsorship Program by CAST, as well as the Shanghai Overseas Leading Talent and Shanghai Pujiang Programs. Her research is centered around a transient high-temperature synthesis platform—a novel approach for rapidly creating advanced materials—and she also brings extensive experience in electrocatalysis, particularly in hydrogen production.

Haijiao Liu, a master's student in Materials Science and Engineering at the University of Shanghai for Science and Technology, is primarily focused on the development and characterization of advanced noble metal-based high-entropy alloy materials synthesized via transient high-temperature processing techniques, with a particular emphasis on their electrocatalytic applications in water splitting.